NPL
National Physical Laboratory

Report

NPL REPORT MAT 12

# Characterization of Nanosized Filler Particles in Polymeric Systems: A Review

W R Broughton

NOT RESTRICTED

January 2008

National Physical Laboratory | Hampton Road | Teddington | Middlesex | United Kingdom | TW11 0LW
Switchboard 020 8977 3222 | NPL Helpline 020 8943 6880 | Fax 020 8614 0446 | www.npl.co.uk

Department for Innovation, Universities & Skills

# Characterization of Nanosized Filler Particles in Polymeric Systems A Review

W R Broughton
Industry and Innovation Division

## ABSTRACT

This report critically examines measurement techniques for determining the shape, size and size distribution of nanosized filler particles in polymeric systems. Particular emphasis has been placed on the ability of these techniques in providing reliable, quantitative data for assessing the level of dispersion in components for production and service inspection purposes, and for use in predicting material properties of nanoparticulate reinforced polymers. The report covers analytical techniques, such as scanning electron microscopy (SEM), transmission electron microscopy (TEM) and scanning tunnelling microscopy (STM), X-ray diffraction (XRD) and X-ray tomography, nuclear magnetic resonance (NMR), atomic force microscopy (AFM) and nanoindentation for laboratory studies. It also considers electrical and electromagnetic (dielectrics, electrical impedance tomography (EIT) and eddy current), optical, rheometric, thermal and ultrasonic techniques potentially suitable for production or service inspection. The measurement techniques are assessed in terms of the data generated, fitness for purpose, ease of use, sensitivity and spatial resolution, and consistency of data.

The report presents an overview of predictive analysis techniques for characterising thermal and mechanical properties of dispersed nanoparticulate polymeric materials. Modelling approaches considered continuum-based modelling including micromechanical models (Halpin-Tsai and Mori Tanaka) used for predicting thermo-mechanical properties of conventional composites, molecular modelling and computational methods used for characterising the behaviour of nanocomposites. The models are discussed in terms of applicability to nano-filled polymeric systems, data provided and ability to accommodate the effects of clustering (i.e. dispersion non-uniformity) resulting from post-processing migration due to electrical, thermal and chemical effects.

ISSN 1754-2979

National Physical Laboratory
Hampton Road, Teddington, Middlesex, TW11 0LW



We gratefully acknowledge the financial support of the UK Department for
Innovation, University and Skills (National Measurement System Policy Unit)

Approved on behalf of the Managing Director, NPL,
by Dr M Cain, Team Knowledge Leader,
authorised by Director, Industry and Innovation Division.

# CONTENTS

# 1 INTRODUCTION

As the pace of nanocomposites research has intensified, it has become apparent that the conventional approach to understanding and optimising material performance of polymeric nanocomposites (PNCs) is not applicable. The misconception is that it is simply a case of scale and that technology applicable to discontinuous reinforced composites is directly transferable to nanocomposites (e.g. nanotube and nanofibre composites). At the nanoscale (1-100 nm), the boundary between a material and a functional device may become blurred [1]. The conventional approach used to determine structure-property relationships is unsuitable when the length-scale of the morphology of the reinforcement and the critical-length of the fundamental physics of a given property coincide (i.e. the onset of non-bulk (localised) properties). Particles with sizes below 100 nm are characterised by extremely large surface-to-volume ratio. For particles with a diameter of 10 nm, 15 % of all atoms are located on the particle surface compared to 0.015% for 1 mm diameter particles. The thickness of a human hair is approximately 10,000 nanometres.

Filler content needed to enhance material performance of PNCs is also on a reduced scale (typically 1-5 vol.%) compared with conventional polymer matrix composites (PMCs). The addition of nanoparticles has a beneficial effect on a wide suite of mechanical and physical properties (e.g. stiffness, strength, thermal stability, fire retardancy, fracture toughness, etc.), improving functionality to levels not achievable using larger scale fillers in the same quantities. These enhancements can be achieved without compromising processibility, weight and cost.

The engineering properties and performance characteristics of complex multiphase polymeric systems, such as PNCs, are dependent upon a number of factors:

- Spatial and compositional nature of the nanoparticulate filler;
- Size, orientation and spatial distribution of the nanoparticles in the matrix;
- Filler and matrix engineering properties;
- Interfacial region between filler and matrix; and
- Constituent volume fractions.

It could be argued that the same factors that influence the performance of PNCs are equally applicable to the performance of conventional composites, but for six interrelated characteristics associated with nanoscopic dimensions and inherent surface areas of nanofillers. These distinguishing characteristics have been identified as [2]:

- Low percolation threshold (~0.1-2.0 vol.%) – critical volume fraction at which an infinite network of randomly dispersed particles form a continuous path across the composite;
- Particle-particle interactions arising at low volume fractions affecting orientation and position of adjacent particles (short range order or correlation);
- High particle density per particle volume ($10^6$-$10^8$ particles/$\mu m^3$);
- High surface (interfacial) area to volume ratio ($10^3$-$10^4$ $m^2$/ml);
- Short inter-particle separation (of the order of 10-50 nm for 1-8 vol.%); and
- Comparable dimensions for particulate particle separation and relaxation volume of polymer chains.

Not all of these characteristics apply to the same degree for all forms of nanofillers. It is self-evident that for spherical nanoparticles the aspect ratio is low, thus it may be argued that oriental correlations between particles is not an issue, however that is not the case. Particle size and inter-particle dimensions are of a similar order of magnitude to the molecular radius of gyration $\mathbf{R_G}$ (10-20 nm), which is the root-mean-square average of the distances of all the molecular segments from the centre of mass of the molecule. Since chain conformations of a polymer sample are quasi-infinite in number and constantly changing over time, $\mathbf{R_G}$ is considered to be the mean value of "radius of gyration" over the entire ensemble of polymer molecules of the sample with time:

$$\mathbf{R_G} = \frac{\mathbf{1}}{\mathbf{N}} \left\langle \sum_{\mathbf{k=1}}^{\mathbf{N}} \left( \mathbf{r_k} - \mathbf{r_{mean}} \right)^2 \right\rangle \qquad \textbf{(1)}$$

where $\mathbf{r_{mean}}$ is the mean position of the monomers.

The radius of gyration is also proportional to the root-mean-square distance between the monomers. The internal interfacial area generated by fully exfoliated and dispersed high aspect ratio plates or rods are comparable to that of macro-molecular dendrimers (spherical polymeric molecules) and proteins. Dendrimers and proteins differ in that proteins are polymers made from 20 different monomers, while dendrimers are polymers made from two monomers: acrylic acid and a diamine with usually an amine core (e.g. ammonia).

**Note:** Fully exfoliated refers to when the mean distance between particles becomes a maximum for a given filler content.

PNCs are intrinsically anisotropic, exhibiting a domain-like structure resembling grains within which these domains have a preferred filler orientation. At a global level, the orientation can be considered isotropic. Small critical concentrations of filler of the order of $10^{-3}$ for plates and $10^{-3}$ for rods can dictate orientation correlation between particles. It also means rapid enhancement of transport phenomena, such as electrical and thermal conductivity, derived from percolation networks, can be achieved for low volume content of high aspect ratio nanoparticles.

The underlying structural-property relationships developed for conventional composites are thus inappropriate, in fact there is far more commonality with meso-structured macromolecular systems, such as semi-crystalline polymers, block-polymers and liquid crystal polymers [1]. There is the additional factor of interaction between nanoparticles and crystalline and amorphous phases, which has an impact on order-disorder transitions (e.g. glass transition temperature $\mathbf{T_g}$), relaxation processes and phase behaviour.

This report critically examines measurement techniques for determining the shape, size and size distribution of nanosized filler particles in polymeric systems. Particular emphasis is placed on the ability of these techniques in providing reliable, quantitative data for assessing the level of dispersion in components for production and service inspection purposes, and for use in predicting material properties of nanoparticulate reinforced polymers.

The report covers analytical techniques, such as scanning electron microscopy (SEM), transmission electron microscopy (TEM) and scanning tunnelling microscopy (STM), X-ray diffraction (XRD) and X-ray tomography, nuclear magnetic resonance (NMR), atomic force microscopy (AFM) and nanoindentation for laboratory studies. It also considers electrical and electromagnetic (dielectrics, electrical impedance tomography (EIT) and eddy current), optical, rheometric, thermal and ultrasonic techniques potentially suitable for production or service inspection. The report consists of six sections including the Introduction (Section 1). Material systems and dispersion parameters are covered in Sections 2 and 3, respectively. Section 4 covers measurement techniques for characterising dispersion and Section 5 reviews predictive analysis techniques. Discussion, general conclusions and recommendations for future work are presented in Section 6.

## 2 MATERIAL SYSTEMS

**Nanoscale Filled Systems**

Nanoscale filled systems cover a wide range of filler and polymeric material combinations:

- Clay/polymer nanocomposites (organoclays)
- Organic-silica hybrids (aluminosilicates and silica nanotube-acrylic)
- $CaCO_3$ (talc)/polymer nanocomposites
- Graphite/polymer nanocomposites
- Carbon nanotubes (single-walled and multi-walled nanotubes)
- Nano-metal particle enhanced polymers

Nanocomposites encompass a large variety of systems made of distinctly dissimilar components and mixed at the nanoscale. The nanophase inclusions vary in degree of complexity from one-dimensional (e.g. single-walled and multi-walled nanotubes (SWNT and MWNTs), and nanofibres) to three-dimensional (3-D) elements (e.g. dendrimer) with different degrees of spatial complexity (e.g. tetrapods) and connectivity. The filler can be in the form of single particles or clusters of particles (e.g. carbon black, silica, mineral fillers and hyper branched polymers).

The morphology of inorganic fillers is typically described as “particulate” (or “conventional”), “intercalated” or “exfoliated” (see Figure 1). In conventional layered structures, the filler (e.g. clay) adopts an aggregated morphology.

In **intercalated** (sandwiched) lamellar (or layered) nanocomposites, the polymer chains alternate with the inorganic layers in a fixed compositional ratio and have a well-defined number of polymer layers in the intralamellar space, potentially accessible by foreign species (Figure 1). Accessibility enables these materials to act as hosts for polymers, yielding interesting hybrid nanocomposite materials. In layered systems, the interface interactions between the two phases are maximised. Two-dimensional layered materials include organo or nanoclays, metal oxides and metal phosphates.

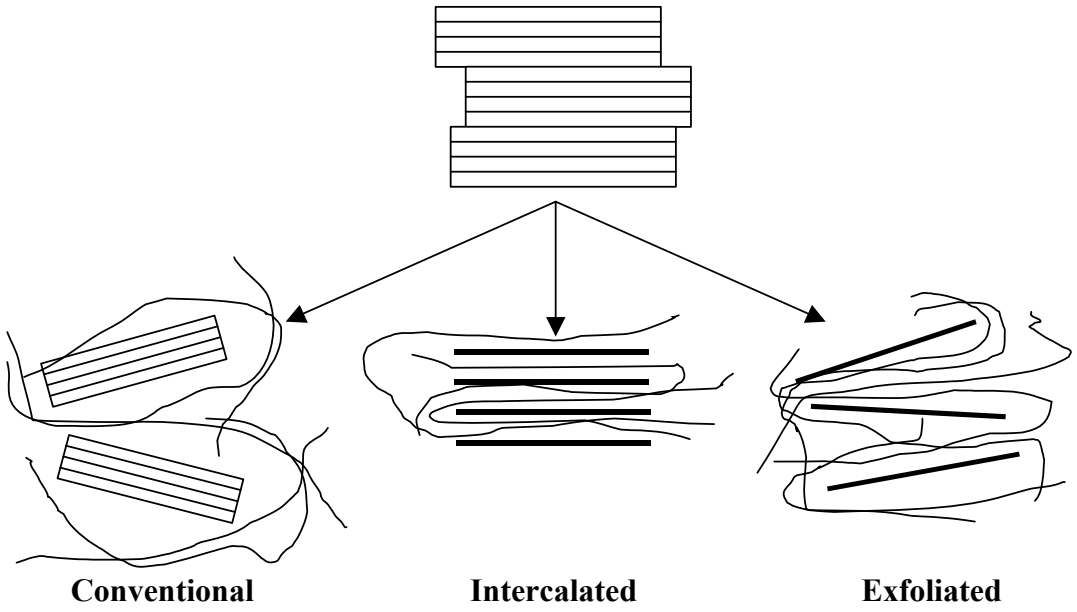


**Figure 1: Schematic illustration of a polymer-layered silicate structure**

**Exfoliation** (delamination) is defined as the dispersion of a layered compound to form highly anisotropic particles and significant amount of individual layers. Better property enhancement is observed when the layered material is exfoliated within the polymer matrix because each nanolayer contributes to the interfacial interactions with the matrix. In exfoliated nanocomposites, the number of polymer chains between the layers is almost continuously variable and the layers stand >100 angstroms apart.

Intercalated nanocomposites are more compound-like because of the fixed polymer/layer ratio. The electronic and charge transport properties that these materials have to offer has attracted industrial interest. On the other hand, exfoliated nanocomposites have superior mechanical properties.

**Nanoclays** [3-4], such as montmorillonites (layered aluminosilicate mineral with sodium counter ions present between the clay layers) are one of the most widely used nanofiller materials. These materials are known to enhance mechanical and thermal properties, and flame retardancy when added to polymers, such as epoxies, polyolefins (with limited success), polystyrenes, polyamide-6 and polysulfones. In nature these materials form a closed structure, which needs to be exfoliated in order to optimise mechanical performance.

Exfoliation results in platelets with a thickness of one nanometre and with lateral dimensions of 50 to 100 nanometres (a surface area of 700 $m^2/g$). Compatibility with polymers is usually achieved through ion exchange of the sodium counter ions with organic ammonium or phosphonium salt to convert the material into a hydrophobic ammonium- or phosphonium- treated clay. A number of techniques have been employed for producing nanoclay composites including blending processes (i.e. melt blending and solution blending), reactive solvent approach and by a polymerisation process.

# 3 PROCESSING

## 3.1 PROCESSING ISSUES

The efficiency of mechanical mixing is dependent on the matrix viscosity and reactivity. Insufficient mixing will result in hybrid micron-scale reinforcement with distinctive localised heterogeneity. The result is a material that is similar to that of conventional filled systems. The aim is to produce a well-dispersed uniform distribution of nanoreinforcement in which nanoparticle separation is maximised, thus providing a particulate filled material that behaves essentially as an isotropic filled polymer. Key parameters to be considered include:

- **Rheology (flow behaviour)** of suspensions of rigid particles in the liquid-melt. The presence of particles increases the intrinsic viscosity of the fluid. An increase in viscosity tends to be minimal in many cases due to the low volume fractions of filler used in producing nanocomposites.

- **Dispersion**: It is very difficult to mix fine powders into highly viscous polymer melts to produce a uniform dispersion. Dispersion is partially dependent on the intensity and time of mixing. Entrapment of air may also occur during mixing, particularly within poorly dispersed regions (i.e. particle agglomerates or clusters), thus compromising material performance (i.e. stiffness and strength).

Examination of the experimental data and observations presented in published literature clearly indicates major inconsistencies – a reflection in part on the variability in sample quality within a batch and between batches of samples. These inconsistencies can be attributed to a number of factors listed below:

- Variable specimen preparation methods
- Variations in nanofiller quality and purity
- Contaminants and voids
- **Degree of dispersion**
- Type and aspect ratio of fillers
- Degree of alignment (i.e. orientation)
- Differences in filler-polymer interfacial chemistry (reactivity)

**Note:** Ultrasonic methods, such as low energy ultrasonication, can aid dispersion.

The basic objective in preparing a nanocomposite is to fully disperse the filler uniformly throughout the polymer matrix. For some thermoplastics nanofillers are best introduced at the polymerisation stage, but considerable research has been carried out to provide compatible filler chemistry so that they can be added at the melt compounding stage. The biggest drawback of the polymerisation method is that only large material suppliers have the equipment to produce sufficient quantities of material. The melt compounding approach is a far more convenient method and significant property enhancement can still be obtained by using this method.

**Technical Issues Associated with Processing**

Technical issues associated with processing to be resolved:

- Interaction between processing variables and nanostructure
- Process-history dependencies
  - **Nanoparticle networking and percolation**
  - **Irreversible nanoparticle aggregation**
  - Polymer crystallinity dependence on filler type and content
- Process-induced orientation
  - Alignment techniques (filtration/deposition)
- Molecular dynamics (relaxation processes)
- Molecular modelling

## 3.2 DISPERSION

The dispersion of nanoparticles in polymeric materials during the mixing process has proven difficult with the result often being phase separation and agglomeration (i.e. clustering - non-uniform dispersion) as indicated in Figure 2. Post-processing migration of nanoparticles may also occur due to electrical, thermal or chemical effects resulting in clustering.

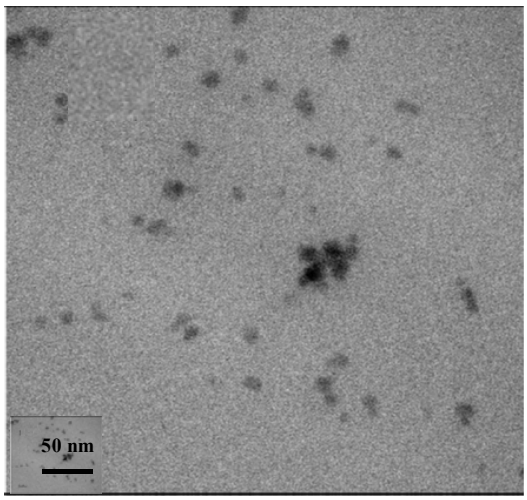


**Figure 2: TEM image of silica nanoparticulate reinforced PMMA (1.2% w/w)**

For an evenly dispersed nanocomposite system with uniform sized spherical particles, the inter-particle distance **l** can be expressed as [5-6]:

$$\mathbf{l} = \mathbf{r}\left[\left(\frac{4\pi}{3V_f}\right)^{1/3} - 2\right] \qquad \textbf{(2)}$$

where **r** is the radius of the particle and $\mathbf{V_f}$ is the volume fraction. Generally there will be variations in particle size and some degree of agglomeration. Clustering of nanoparticles can arise due to the presence of a short-range attractive force among the particles.

Statistical functions, such as Poisson point field [7] have been used to describe random point patterns for quantification of dispersion. Poisson point field approach describes the complete spatial randomness in fibre distribution. This means that the probability of finding **N** particles or fibres in a sub-domain of area **A** is the same for any chosen sub-domain. Consequently, the model assumes no agglomeration of particles in the composite. The probability of finding **k** particles in a window **W** of area **A(W)** is given by [7]:

$$\mathbf{P[N = k] = r\frac{(\lambda \cdot A(W))^k}{k!} \cdot e^{-\lambda \cdot A(W)} k = 0,1,...} \quad \textbf{(3)}$$

where $\lambda$ is the fibre density (fibres per unit area).

A major concern is that Poisson distribution is physically unattainable due to the finite dimensions of the inclusions. Poisson distribution is often used for comparison purposes to distinguish between aggregated and more regular patterns. In an attempt to accommodate real situations, the inclusions are assigned a finite radius (referred to as Matérn's model [7] – describing random position of fibres within the composite). In this case, the centre between two inclusions cannot be closer than the particle diameters. The pair distribution function **g(r)** can be defined as the probability of finding an inclusion whose centre lies within an infinitesimal circular region of radius **dr** around the point **r**, provided that the coordinate system is located at the centre of a second inclusion.

An alternative statistical approach is to employ Ripley's K-function [7-8] to discriminate between different particle (fibre) distributions. This function can be defined as the number of further points expected to lie within a radial distance **r** of an arbitrary point and divided by the number of points per unit area. Ripley's estimator **K(r)** (or second order intensity function) is defined as [7]:

$$\mathbf{K(r) = \frac{A}{N^2} \sum_{k=1}^{N} w_k^{-1} \cdot I_K(r)} \quad \textbf{(4)}$$

where **N** is the number of points in the observation area **A**, $\mathbf{I_K(r)}$ is the number of points lying within the circle of radius **r** and with the centre located in the **kth** point and weight $\mathbf{w_k}$ is the proportion of the circumference contained within the sampling area **A** to the whole circumference with radius **r**. The weight $\mathbf{w_k}$ can be computed numerically or using analytical expressions (see [9]).

The relation between pair distribution function **g(r)** and **K(r)** is given as [10]:

$$\mathbf{g(r) = \frac{1}{2\pi r}\frac{dK(r)}{dr}} \quad \textbf{(5)}$$

Although the two functions are related, **g(r)** and **K(r)** provide distinctively different physical information. **K(r)** can distinguish between different patterns and detect regularities, whereas as **g(r)** describes the occurrence intensity (frequency) of inter-inclusion distances (i.e. local maximum indicates the most frequent distances between points and a local minimum the least frequent ones in the pattern). The two functions are useful in describing long-range interactions between points.

In order to discriminate between different fibre distributions (see Figure 3) and for quantification purposes, it is recommended that **K(r)** be reduced to some appropriate scalar value [8]. A micro-structural parameter $\chi$, which is indicative of the deviation of a given pattern from complete randomness, has been suggested for this purpose. This is based on the averaging of the ratios between **K(r)** of a given microstructure and $\pi r^2$. Micro-structural parameter $\chi$ is defined as [8]:

$$\chi = \frac{1}{b-a}\int_a^b \frac{K(r)}{\pi r^2}dr \approx \frac{1}{m}\sum_{i=1}^{m}\frac{K(r_i)}{\pi r_i^{\,2}} \qquad (6)$$

where [**a**, **b**] is the length scale range of interest (i.e. **a** is the particle or fibre diameter and **b** is larger than the largest cluster size). Particle distributions can be computed using the Metropolis Monte Carlo method.

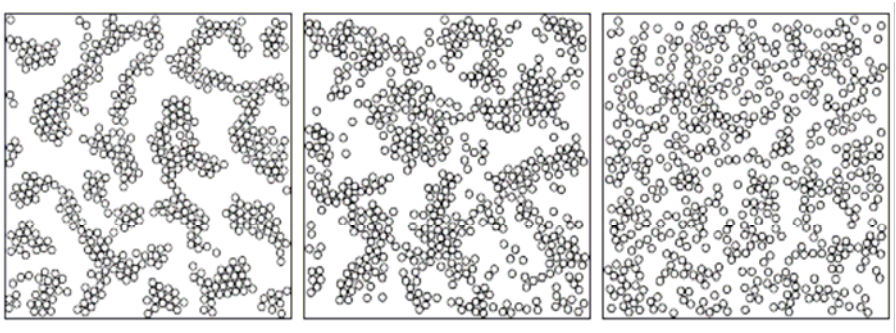

**Figure 3: Particle dispersion: highly aggregated (left) to fully dispersed (right) [8]**

## 3.3 ORIENTATION DISTRIBUTION

The analysis discussed in Section 3.2 assumes an evenly dispersed nanocomposite system with uniform sized spherical particles, whereas in reality most nanocomposites have anisotropic shaped particles (e.g. nanotubes and platelets). The particle (or fibre) orientation distribution is an important parameter in determining the mechanical performance of the composite because most material properties are highly dependent on this aspect of the materials microstructure. Quantitative data relating to orientation distribution can be determined using 2-D image analysis methods developed for continuous and discontinuous fibre-reinforced composites [11-12].

The orientation of a single fibre is described in polar coordinates by two angles, $\theta$ and $\phi$. Alternatively, the orientation of individual particles can be characterised by the components of a vector **p**, which lies parallel to the major axis of the fibre (Figure 4). The components of the second-order orientation tensor $\mathbf{a_{ij}}$ describing the orientation state of **n** fibres are given in Equation (7) [11-12].

$$a_{ij} = \frac{1}{n}\sum_{i=1}^{n} a_{ij}^{k} = \frac{1}{n}\left(\sum_{i=1}^{n} p_i^k p_j^k\right) = \begin{pmatrix} a_{11} & a_{12} & a_{13} \\ a_{21} & a_{22} & a_{23} \\ a_{31} & a_{32} & a_{33} \end{pmatrix} \quad i,j = 1,2,3 \qquad (7)$$

where $p_i^k p_j^k$ is a dyadic product of the **kth** fibre's vector components.

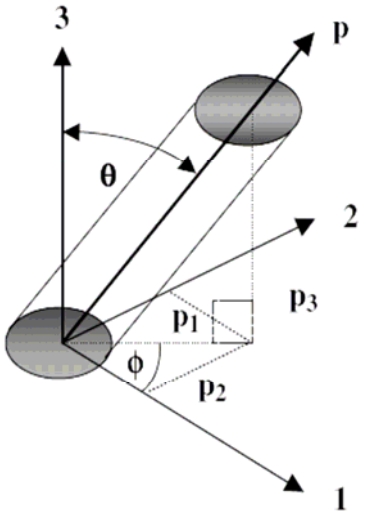


**Figure 4: Orientation of a single fibre expressed in polar coordinates (θ, ϕ) and cartesian coordinates by the components of vector p, ($p_1$, $p_2$, $p_3$)**

The probability that a randomly located section plane will intersect a fibre is related to the fibre length **L**, diameter **D** and the orientation (i.e. with the section plane **θ**) as follows [11-12]:

$$\mathbf{P(\theta) = L\cos\theta = D\sin\theta} \tag{8}$$

In order to derive an estimate of the orientation tensor, the tensor components of each fibre **k** must be weighted by the inverse of its probability of intersection $\mathbf{F^k}$ (inverse of **P**). The resultant weighted orientation tensor is given by [11-12]:

$$\mathbf{a_{ij}} = \frac{\sum_{i=1}^{n} \mathbf{F^k a_{ij}^k}}{\sum_{i=1}^{n} \mathbf{F^k}} \tag{9}$$

The orientation of a fibre and the location of its intersection with the section plane are described by the parameters ($\theta^k$, $\phi^k$) and ($x^k$, $y^k$), respectively. Fibre orientation is derived from the elliptical cross-section as follows [11-12]:

$$\theta^k = \arccos(b/a)$$
$$\phi^k = \phi \text{ or } \phi + 180° \tag{10}$$

where terms **a** and **b** are the major and minor axis lengths of an ellipse and **ϕ** is the in-plane orientation angle. Note that fibres with orientations **ϕ** and **ϕ + 180°** have identical cross-sections. A number of different automated techniques for measurement of elliptical parameters by binary image analysis have been developed including least squares and second moments techniques, which have been shown to give similar results (see [11-12] for further details). Errors are known to increase as $\theta \rightarrow 0$.

### 3.4 LENGTH DISTRIBUTION

At the synthesis level, it is difficult to control the morphology (including length) of nanoparticles. Modelling the effective behaviour of finished products is complicated due to the complex micromechanical characteristics and length distribution of the nanoparticle reinforcement. The final mechanical properties of a finished product, such as tensile strength, elastic modulus, and fracture toughness, are critically dependent on the entire length distribution rather than the simple mean length. The length distribution can often be characterized with either a Weibull or log-normal distribution.

A useful graphical technique to assess whether or not a length data set follows a given distribution is a probability plot in which the experimental data are plotted against expected values derived from a theoretical distribution. The measurement of nanoparticle length may be carried out using either AFM (e.g. tapping mode) or TEM in conjunction with image analysis software. There will generally be a limited number of particles (<100) in each sample, and hence a large number of samples will be required in order to determine the length distribution for the nanocomposite. This comment also applies when determining orientation distribution. If the theoretical distribution is a good fit, then the points should form approximately a straight line. It is recommended that several distributions be tried in order to identify the distribution that shows the closest fit to the measured length distribution (see [13]).

**Note:** It is not sufficient to be reliant simply on the average length or orientation for modelling purposes. Mechanical performance is critically dependent on the entire length and orientation distributions.

## 4 MEASUREMENT TECHNIQUES

This section examines measurement techniques for determining spatial and temporal distribution of nanoparticles in polymeric materials. It considers analytical techniques (i.e. TEM, XRD and AFM) suitable for laboratory studies and non-invasive techniques (i.e. dielectric, optical and ultrasonic methods) that could potentially be used for production or service inspection. Figure 5 shows the spectrum of measurement techniques as a function of length-scale.

| | | | | | |
|---|---|---|---|---|---|
| **AFM<br>EELS<br>LEEDS<br>TEM** | **AES<br>Nanoindentation<br>SAM** | **SIMS<br>XPS** | **EDX** | **μ-Raman<br>SEM** | **μ-FTIR<br>μ-XRD<br>Optical imaging** |
| **Atomic<br>$10^{-10}$** | **$10^{-9}$** | **Nano<br>$10^{-8}$** | **$10^{-7}$** | **Micro<br>$10^{-6}$** | **$10^{-5}$** |

**Figure 5: Spectrum of measurement techniques as a function of length-scale**

### 4.1 X-RAY DIFFRACTION (XRD)

XRD is a versatile, non-destructive technique that can provide a wealth of information on the structural, physical and chemical nature of natural and manufactured materials. It is commonly used for characterisation of the structure of PNCs providing detailed information on the extent of intercalation and exfoliation in these materials.

**Principle of Operation:** A crystal lattice is a regular 3-D distribution (cubic, rhombic, etc.) of atoms in space. These are arranged so that they form a series of parallel planes separated from one another by a distance **d**, which varies according to the nature of the material. For any crystal, planes exist in a number of different orientations - each with its own specified-spacing. When a monochromatic X-ray beam with wavelength $\lambda$ is projected onto a crystalline material at an angle $\theta$, diffraction occurs only when the distance travelled by the rays reflected from successive planes differs by a complete integer **n** (**n** = 1, 2, 3, etc.) of wavelengths. By varying the angle $\theta$, the Bragg's Law conditions are satisfied by different d-spacings in polycrystalline materials.

$$\mathbf{d}_{00n} = \frac{n\lambda}{2\sin\theta} \qquad \textbf{(11)}$$

Plotting the angular positions $2\theta$ and intensities of the resultant diffracted peaks of radiation produces a pattern, which is characteristic of the sample. The step size is typically 0.005 degrees with a dwell time of approximately 0.05 to 1 second. Where a mixture of different phases is present, the resultant diffractogram is formed by addition of the individual patterns. Based on the principle of XRD, a wealth of structural, physical and chemical information about the material investigated can be obtained. Most X-ray machines use Cu-K$\alpha_1$ radiation with $\lambda = 0.154062$ nm.

**Note:** X-rays are a form of electromagnetic radiation with a wavelength in the range of 10 to 0.01 nm, corresponding to frequencies in the range 30 to 30 000 PHz (1 petahertz = 1015 hertz).

Wide angle X-ray scattering or diffraction (WAXS or WAXD) provides high-resolution diffraction patterns in a broad angular range whilst small angle X-ray scattering or diffraction (SAXS or SAXD) operates at very low angles (0.1 to 10°). Figure 6 shows a Siemens D500 diffractometer. SAXS can be used to determine the microscale or nanoscale structure of particle systems in terms of averaged particle sizes, shapes, distribution, surface-to-volume ratio and characteristic distances of partially ordered systems. It is capable of providing structural information of macromolecules or particles between 5 and 25 nm in size and repeat distances in partially ordered systems of the order of 150 nm. In combination, the two techniques can be used to provide information on molecular orientation.

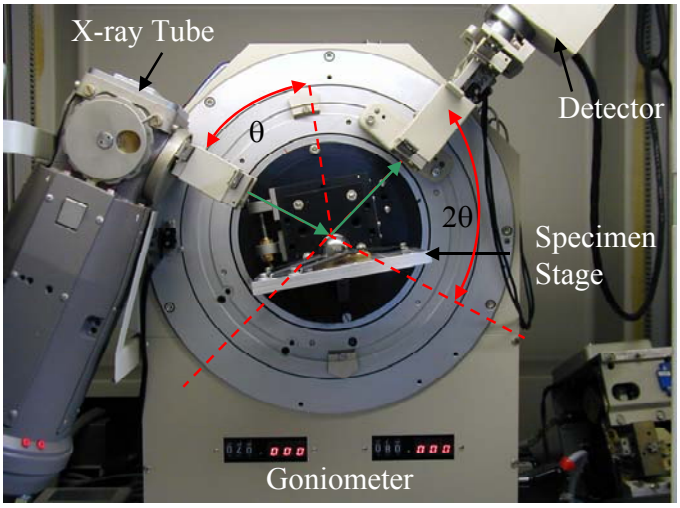


**Figure 6: Siemens D500 Diffractometer**

XRD data obtained for polymers (e.g. polystyrene) containing intercalated organoclay show a distinct peak at low diffraction angles ($2\theta \leq 10°$) [14]. The positions and shapes of the peaks provide information on the structure of the diffracting species (e.g. organoclay). Multiple peaks may occur as a result of different states of change in the diffracting species resulting from incomplete intercalation during mixing of the filler and polymer. For an intercalated structure, the characteristic X-ray peak associated with interlayer spacing $d_{001}$, as determined using Braggs Law (Equation (11)), tends to shift to a lower angle regime due to the expansion of the basal spacing [15]. It is possible to directly relate the peak position $2\theta$ to the interlayer spacing $d_{001}$, and the intensity of the diffraction peak $I_\alpha$ to the concentration of scattering particles. In the case of clay based PNCs, there is a straight-line relation between $d_{001}$ and $1/2\theta$ [14].

Peak broadening has been associated with an increase in the degree of exfoliation, and hence attempts have been made to relate the area under the peaks to the degree of exfoliation [16]. However, peak broadening may be attributed to other factors, such as multiple diffraction peaks from two or more sub-structures of the filler where the differences in diffraction angles are small and overlap. Alternatively, crystalline defects in individual platelets within the stack, as in the case of organoclays, may cause peaks to broaden. In contrast, the absence of diffraction peaks is a possible indication that the system is fully exfoliated or delaminated (i.e. loss of structural order of the layers) [17]. Interpretation of XRD data is difficult and susceptible to error. The technique cannot be used to determine the distribution of silicate in clay-based PNCs.

## 4.2 X-RAY TOMOGRAPHY

X-ray computed tomography (CT) is a rapidly evolving technique originally developed for medical applications enabling visualization of soft-tissues and bones. Current systems can accommodate objects as large as a typical engine block, and portable systems can image objects the size of a small apple. CT has subsequently been adapted and extended to a wide variety of material science applications including nanocomposites. Characteristics of the internal structure of an object such as dimensions, shape, internal defects and density are readily available from CT images. Commercial instruments can provide non-destructive 2-D and 3-D maps of X-ray attenuation of material samples. Basic CT configurations consist of an X-ray source, a sample through which the X-ray pass and a detector assembly, which measures the X-ray attenuation of the X-ray path through the sample. By rotating the sample (or source-detector assembly) many different pathways are measured, obtaining information on X-ray attenuation by filtered back projection for a 2-D slice (fan beam operation). Subsequent acquisition of many such slices results in a 3-D image of X-ray attenuations used to calculate a 3-D reconstruction of the sample.

Recent developments have resulted in CT systems that are able to operate in volume mode (cone beam operation) enabling acquisition of 3-D images of X-ray attenuations with one set of rotations, resulting in very fast measurements. This mode of operation, however, is prone to increased distortion and a reduction in resolution. Actual resolution is limited by several factors, including the X-ray magnification and the number of pixels of the detector. In addition, it is currently feasible to reconstruct images up to 1024 x 1024 x 1024, which is the limit of the computational capability.

In practice, this implies that samples of 2 cm diameter and 2 cm height can be resolved with voxels (3-D equivalent to pixels) of 20 μm, while smaller samples can yield voxel sizes approaching 3 μm. CT technology has been further improved by the use of microfocus X-ray sources in the computer tomography equipment. In microfocus computer tomography (μCT), the resolution of a system can be in the order of 10 μm x 10 μm x 10 μm depending on the object size. Although the technique is a powerful and versatile inspection tool, its main drawback at present is its high investment cost and limited resolution with respect to length-scales associated with nanocomposites.

## 4.3 SCANNING ELECTRON MICROSCOPY (SEM)

This is the most widely used of the surface analytical techniques. High resolution SEM has proved an invaluable tool for studying surface topography, nanoparticle structures (e.g. SWNTs and MWNTs) and failure analysis. The technique enables qualitative 3-D imaging of surface features, however, it does not easily lend itself to quantitative surface roughness characterisation. This can be overcome by complementing SEM investigations with AFM. In SEM, a highly focused scanning electron beam bombards the surface causing large numbers of secondary electrons to be generated, the intensity of which is governed by surface topography. The sample is bombarded with electrons to visualize the surface, which is constantly scanned and reconstructed. A detector collects a part of the emitted electrons and an image is built by signal modulation and amplification.

The method is suitable for all materials, but non-conducting materials must be coated with a thin conductive layer (e.g. gold sputtered), which can alter or mask the true surface morphology. The resolution of topographical features is ~2 to 5 nm. SEM is often used to survey a surface before more specialised techniques are employed. With the addition of energy dispersive X-ray spectrometry (EDX or EDS), the SEM can also be used as an elemental analysis tool.

EDX involves analysis of the elemental composition of a surface from X-rays emitted upon exposure to a primary beam of electrons. The X-rays emitted are characteristic of the atom from which they originated. Detection and analysis of characteristic X-ray lines of various elements can be obtained using an EDX system attached to an SEM. The maximum operational depth of EDX is typically 2 to 10 mm and the volume analysed can be as large as several cubic microns. The actual penetration depth depends on the type of material being analysed and the acceleration potential used in the SEM. The technique can be used generate elemental distribution maps of the area of interest, enabling both qualitative (boron to uranium) and quantitative (sodium to uranium) elemental analysis. The technique cannot provide information on chemical bonds, although it can provide information on element depletion and migration as a result of environmental exposure.

## 4.4 TRANSMISSION ELECTRON MICROSCOPY (TEM)

TEM is a powerful imaging tool that is widely used as a research tool for characterisation of materials at the nanoscale. The technique can be used to determine the shape and distribution of nanoparticles and has a spatial resolution on the atomic scale sufficient in many cases to resolve the external and internal structure of nanoparticles (e.g. MWNTs – see Figure 7). Spatial resolutions of 0.1 nm (or even 0.05 nm) are achievable with modern instruments. The basic principle of operation is a beam of electrons is transmitted through the specimen, forming an image of the subject, which is magnified and directed onto a fluorescent screen or layer of photographic film, or in modern instruments detected by a sensor such as a CCD (charge-coupled device) camera. A TEM can be modified into a scanning transmission electron microscope (STEM) by the addition of a system that rasters (scans) the beam across the sample to form the image, combined with suitable detectors.

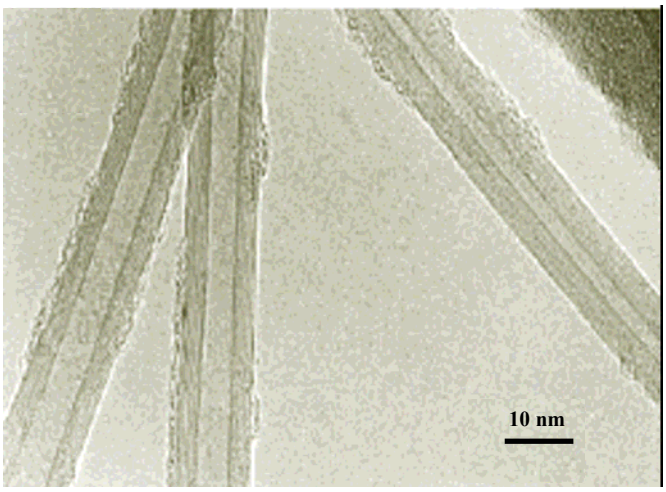


**Figure 7: TEM image of multi-walled nanotubes**

A major disadvantage is the extensive sample preparation required in order to produce sufficiently thin samples that are transparent to electrons, and hence analysis is a relatively time-consuming process with a low throughput of samples. The structure of the sample may also be altered (or damaged) during the preparation process or when exposed to the electron beam. Biological samples are particularly vulnerable. Also the field of view is relatively small, raising the possibility that the region analysed may not be characteristic of the whole sample.

## 4.5 SCANNING TUNNELLING MICROSCOPY (STM)

STM has revolutionised surface science enabling real space atomic resolution images of surfaces [18-20]. The technique consists of rastering a conductive sample with a fine metallic tipped probe with the probe in close proximity to the sample surface. A voltage is placed between the probe tip and the sample surface. As the probe tip approaches to within 10-20 nm of the surface, a tunnelling current (0.01-50 nA) can be induced in either direction between the tip and the surface with current flow being sensitive to the distance between the tip and the surface, and conductivity of the sample.

The exponential dependence of the tunnelling current on the probe tip to surface distance results in a high vertical resolution. The current between the probe tip and sample surface is continuously monitored and by maintaining a constant current (**constant current mode**) it is possible to generate a topographic image of the surface. As the current is proportional to the local density of atomic states, the probe tip follows a contour of constant density of atomic states during scanning.

**Constant current mode** of operation is only suitable for atomically flat surfaces otherwise the tip would inevitably collide with the surface damaging the probe tip and sample. A conductive sample is needed to generate a current flow between probe tip and sample surface. The STM needs to be operated under ultra high vacuum (UHV) conditions in order to produce atomic resolution images. In **constant current mode**, image generation is slow. A single image may require seconds to a few minutes to generate.

Typical spatial resolution is 3 nm with a vertical feature resolution of < 0.1 nm. A wide range of scan sizes from 100 μm down to the atomic level can be covered in a single experiment. Hence, it is possible to obtain an overview image of the surface and then zoom-in on structural features at higher resolution to investigate local defects, such as dislocations. Although STM measurements are usually undertaken in UHV conditions, STMs can also be operated under ambient conditions.

## 4.6 SCANNING PROBE MICROSCOPY

**Scanning Probe Microscopy (SPM)** describes any technique where the surface is imaged at high (or atomic scale) resolution by rastering (or scanning) an atomically sharp tip in close, but not in direct contact (see Figure 8) [18]. The measurement of the interaction between the probe tip and surface is combined with the measurement of the relative position of the probe tip to produce an image of the interaction strength as a function of position in the x-y plane and providing information on surface topography, lateral force, conductance, magnetic attraction or electrochemical response.

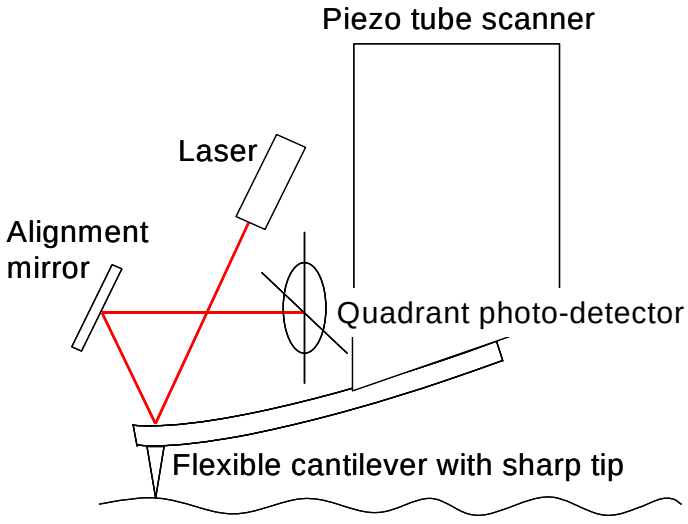


**Figure 8: Schematic of scanning probe microscope**

**Atomic Force Microscopy (AFM)** is a subset of SPM and measures surface characteristics, such as topography (Figure 9), on the atomic scale [21-26]. A small tip mounted on a flexible cantilever attached to a measuring device is used to analyse the small vertical movements of the probe as it travels over the contours of the surface of the sample (similar principle of operation to the stylus profilometer). The cantilever is typically silicon or silicon nitride (typically 100-200 μm in length) with a tip radius of curvature of the order of 5-10 nm.

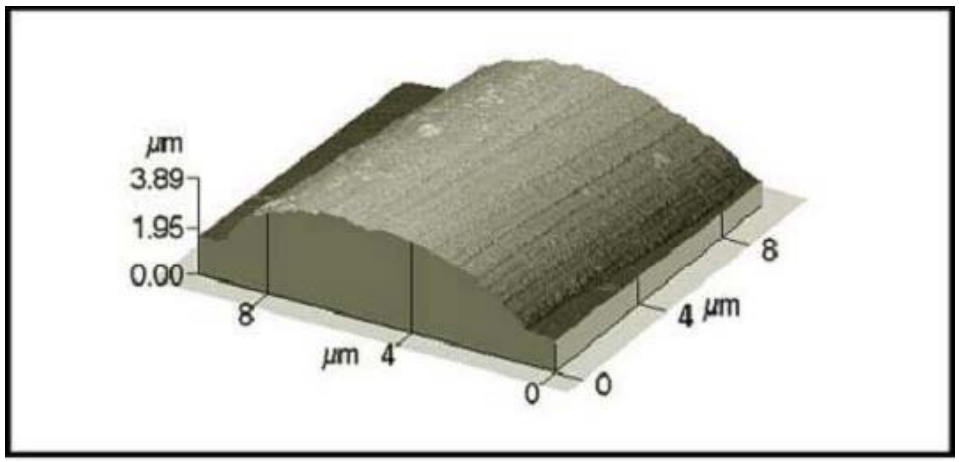


**Figure 9: AFM surface map of a treated carbon fibre [21]**

The surface deflection of the cantilever, caused by changes in topography or surface adhesion, is usually measured using a laser spot reflected from the top of the cantilever into an array of photodiodes. The deflection of the cantilever behaves according to Hooke's law. Optical interferometry, capacitive sensing and piezoresistive AFM probes are also used for measuring deflection. These probes are fabricated with piezoresistive elements that act as a strain gauge. A Wheatstone bridge is used to monitor strain in the AFM probe due to deflection, but this method is not as sensitive as laser deflection or interferometry. A feedback mechanism is generally employed to adjust the tip-to-sample distance to maintain a constant force between the tip and the sample, and also to prevent the tip colliding with the sample and damaging the tip. High-resolution scans can take some time, and effects from thermal drift and probe shape de-convolution must be considered.

AFM has a spatial and depth resolution of the order of a few nanometres. Maximum scan range is typically 100 μm in the x- and y-directions, and 7 μm in the z-direction. Forces of the order of a few pico-newtons can now be routinely measured. AFM can be used to monitor interaction forces, such as van der Waals, magnetic, electrostatic, capillary and chemical bonding forces as a function of the separation distance between the probe tip and the sample surface.

AFM has several advantages over SEM. Unlike the SEM, which provides a 2-D projection or a 2-D image of a sample, the AFM provides a true 3-D surface profile. Additionally, samples viewed by AFM do not require any special treatments (such as metal/carbon coatings) that would irreversibly change or damage the sample. While SEM needs expensive vacuum environment for proper operation, most AFM modes can work perfectly well in ambient air or even a liquid environment. Almost all materials can be studied without the need for sample preparation.

There are two main modes of operation: static (**contact)** and dynamic (**non-contact**), which maintains a constant force or separation to the sample surface, respectively. In **contact mode**, the probe is brought into contact with the surface with a low force (nN to μN) and rastered across the surface; the force between the tip and the surface is kept constant during scanning by maintaining a constant deflection. Measurement of static signals is prone to noise and drift, hence low stiffness cantilevers are used to boost the deflection signal. However, close to the surface of the sample, attractive forces (i.e. lateral (shear) and normal forces) can be quite strong, causing the cantilever tip to "snap-in" to the surface. The combination of lateral and normal forces can result in reduced spatial resolution and may cause damage to soft materials, such as polymer samples, due to scraping between the tip and sample. Consequently, **contact mode** AFM is almost always done in contact where the overall force is repulsive. Atomic resolution images can only be achieved using **contact** mode AFM.

In dynamic mode (i.e. **tapping mode** and **non-contact mode** imaging), the cantilever is externally oscillated, at or close to its resonance frequency with oscillation amplitude ranging typically from 20 to 100 nm. In **tapping mode** AFM, the cantilever tip "lightly" taps on the sample surface during scanning, contacting the surface at the bottom of its swing. Tip-sample interaction forces modify the amplitude, phase and resonance frequency of the oscillating signal with changes in oscillation with respect to the external reference oscillation providing information about the sample's characteristics. By maintaining constant oscillation amplitude, via a feedback loop, a constant tip-sample interaction is maintained during imaging. The vertical position of the scanner at each position in the x-y plane is recorded to form a topographical map of the sample surface. Samples are less prone to being damaged, as lateral forces are virtually eliminated.

In **non-contact mode**, the tip does not contact the sample surface, but oscillates above the surface at a frequency slightly higher than the resonance frequency of the cantilever. Amplitude of oscillation is less than 10 nm. Van der Waals forces, which extend approximately 1 to 10 nm above the surface, interact with the cantilever tip causing the resonant frequency of the cantilever to decrease. The decrease in resonant frequency is accompanied by a decrease in amplitude of oscillation. The feedback loop is used to either maintain constant oscillation amplitude or frequency and the distance the scanner moves vertically recorded to form a topographic image of the sample surface. The advantage of **non-contact mode** AFM is that no force is exerted on the sample surface. Limits on the tip-sample separation results in lower lateral resolution. In order to avoid surface contact, scan speeds need to be reduced, and hence scan speeds are lower than contact and tapping modes.

Schemes for dynamic mode operation include frequency modulation and the more common amplitude modulation [18-19]. In frequency modulation, changes in the oscillation frequency provide information about tip-sample interactions. Frequency can be measured with very high sensitivity and is used for atomic resolution imaging in ultra-high vacuum (UHV) conditions. In amplitude modulation, changes in the phase of oscillation can be used to discriminate between different types of materials on the surface. Figure 10 shows a phase image of the interfacial region between a glass fibre and vinlyester resin matrix. It can be seen that there is a band of modified matrix at the boundary between the two constituents. Amplitude modulation can be operated either in the non-contact or in the intermittent contact regime.

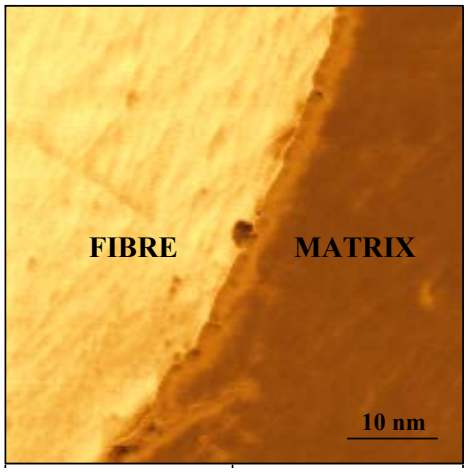


**Figure 10: AFM phase image of glass fibre/vinylester interface**

**AFM nanoindentation** has been used to measure and map nanohardness and elastic modulus [19]. Problems with the technique include no direct measurement of the tip-sample separation and the common need for low stiffness cantilevers, which tend to "snap-in" to the surface. The "snap-in" can be reduced by measuring in liquids or by using stiffer cantilevers, but in the latter case a more sensitive deflection sensor is needed. By applying a small dither to the tip, the stiffness (force gradient) of the bond can also be measured. The radius of curvature of the probe tip limits the quality of an image, and an incorrect choice of tip for the required resolution can lead to image artefacts. Surface contamination and dust can also adversely affect test results.

**Atomic Force Acoustic Microscopy (AFAM)** is a hybrid acoustic/AFM technique that involves vibrating the cantilever at ultrasonic frequencies (10 kHz – 10 MHz) to excite its mechanical resonances [27-33]. The resonant frequencies of the AFM cantilever shift when the cantilever tip is in contact with the sample surface. AFAM can be used to obtain elastic property data. The cantilever can be considered a miniaturised elastic beam that can vibrate in different types of modes (i.e. flexural, torsional and extensional). A piezoelectric ultrasonic transducer is used to excite either longitudinal or shear acoustic waves in the sample under examination. Longitudinal and shear waves cause out-of-plane surface vibrations and in-plane surface vibrations in the sample, respectively. Surface vibrations are coupled to the AFM cantilever beam through the tip when it is in contact with the sample. The AFM photodiode sensor using a lock-in amplifier detects changes in the amplitude of the cantilever vibration.

As the excitation frequency approaches the resonance frequency of the cantilever, the detected amplitude of the cantilever vibrations increases, enabling its resonance frequency to be determined. The amplitude and phase of the cantilever vibration, as well as the shift of the cantilever resonance frequencies contain information about local tip-sample contact stiffness. Quantitative elastic property data can be extracted by measuring the resonant frequencies under both free-space and surface-coupled conditions. Elastic forces dominate tip-sample interactions. AFAM systems are fitted with small diameter tips capable of lateral resolutions of 5-10 nm. Frequency-tracking electronics have been developed to enable rapid imaging of the contact resonance frequency in a given area on the sample surface, thus enabling maps of the contact stiffness and the indentation modulus to be obtained.

In order to generate reliable quantitative data, further work is required to understand and control tip wear and tip-contact sample behaviour. Silicon tips have been known to experience considerable wear during testing, which can cause large uncertainties in elastic property measurements. Using diamond-coated tips, however, the wear can be avoided (or at least minimised). Tip abrasion/erosion and deformation can limit measurement accuracy. Concerns also exist about the effects of viscoelastic damping and the need for finite element analysis (FEA) to account for geometric effects on the resonant frequency for cantilever beams.

## 4.7 NANOINDENTATION

In contrast to conventional hardness methods, instrumented nanoindentation testing has the ability to measure the indenter penetration, **h**, under the applied force, **F**, throughout the testing cycle (i.e. as a function of time), and is therefore able to measure both the plastic and elastic deformation of the material under test [34-35]. As the force is increased, the instrument measures both the plastic and elastic deformation of the material under test. As the force is removed, the indentation recovers elastically and the stiffness of the contact may be related to the elastic modulus of the material under test using knowledge of the area of contact. It is possible to infer the size of an indentation from the measured penetration depth. Instrumented indentation renders a separate measurement of the indent size unnecessary and allows indentation testing at indent sizes much smaller than previously possible using conventional methods. As with conventional indentation testing, knowledge of the indenter geometry is required.

For most hardness measurements an indentation load of 30 N (or greater) is used and the size of the indentation is approximately 300 μm in size in the plane of the tested surface. Nano-hardness testing involves smaller indenters and significantly smaller loads (100 μN to 100 N). The corresponding indentation is far smaller (100 nm or less) and is associated with local properties, whereas standard hardness tests provide bulk hardness measurements of the surface region. Indentations of the order of 10 nm are not uncommon**.** Higher force instruments are now available with the capability of applying forces up to 1500 N**.** Instrumented nanoindentation is one of the very few techniques that can measure both the elastic and plastic properties of very small volumes of materials.

The principle of a typical instrumented nanoindentation system is shown in schematic diagram in Figure 11 [35]. The indenter is mounted on an indenter shaft, which is suspended by flexure elements and is pressed against the test sample by a force actuator (electromagnetic, electrostatic or piezoelectric system). A parallel plate capacitor is commonly used to measure the displacement of the shaft (and therefore the indenter) into the sample. Instrumentation of the indentation displacement removes the need to inspect the indents in order to determine indent size, and thus indents can be much smaller in size.

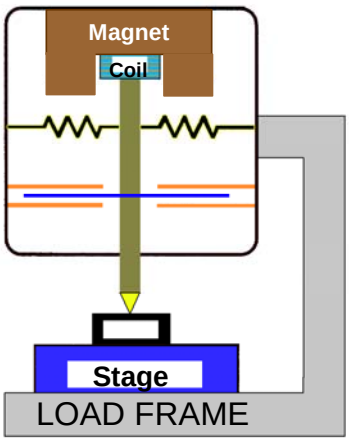


**Figure 11: Schematic of instrumented indentation test system [35]**

For large indents in the upper microindentation range (**h** > 6 μm), the indentation area of contact can be calculated from measurements of indentation depth assuming the indenter has the "ideal" or "perfect geometry" [35]. The error in area is less than 1% for a Vickers or Berkovich indenter that complies with BS EN ISO 14577-2 [36]. For smaller indent depths (i.e. 0.2 μm ≤ **h** ≤ 6 μm), more detailed knowledge of the indenter shape, as a function of depth is required. The key parameter $\mathbf{A_S}$, known as the "area function" (i.e. area as a function of depth) can be determined using a traceably calibrated AFM. The area function needs to be calibrated for each indenter.

In a typical quasi-static indentation cycle, force is progressively applied and the indenter is steadily pressed into the sample. As a result, the sample deforms elastically and plastically under the indenter until a maximum force is reached. The force is often held for a short period of time before being progressively removed with the sample relaxing elastically as the indenter is removed from the surface. Applied force and displacement is recorded either continuously or at frequent time intervals throughout the loading-unloading cycle (see Figure 12). The force-displacement response on its own can provide considerable information, for example, the ratio of the areas under the force loading and unloading curves is an immediate indicator of the balance between elastic and plastic deformation of the material under test.

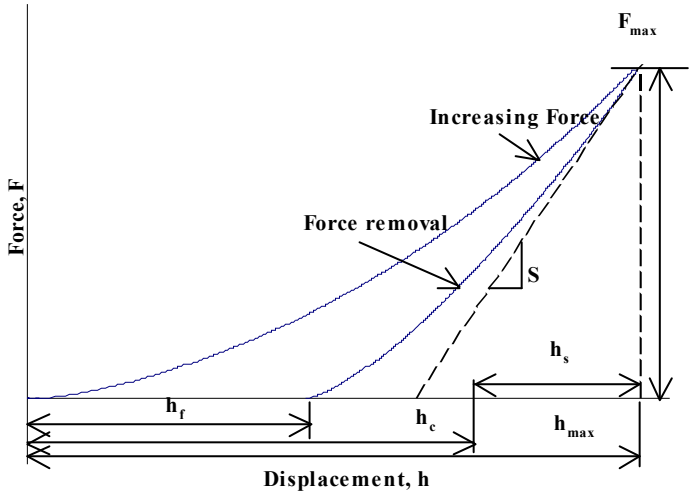


**Figure 12: Typical force-displacement curve**
**Measured (P, $P_{max}$, h, $h_{max}$, $h_f$) and derived parameters (S, $h_s$, $h_c$) [35]**

Figure 13 shows a schematic representation of the indent at maximum applied force and after the force has been removed (after Oliver and Pharr [37]). The overlay in the schematic diagram shows the elastic response as a combination of the sample and the indenter, which can be considered as two springs in series. The gradient of the force-displacement curve as the force is removed is a measurement of the contact compliance **C** (= **1/S**) from which the contact depth, $\mathbf{h_c}$, can be calculated by taking into account the bowing of the surface in response to the exact shape of the indenter. **S** is the slope of the tangent of the force-displacement (indentation) curve during the unloading cycle (Figure 12). Surface bowing is calculated using contact mechanics equations [38-39]. In reality, the actual contact depth is also a function of the test material response to indentation. Sinking-in and piling-up of the material around the indenter can affect the value, reducing and increasing the actual contact depth, respectively. Both phenomena are a function of material processing history and, as in conventional hardness testing, are not included in the standard analysis.

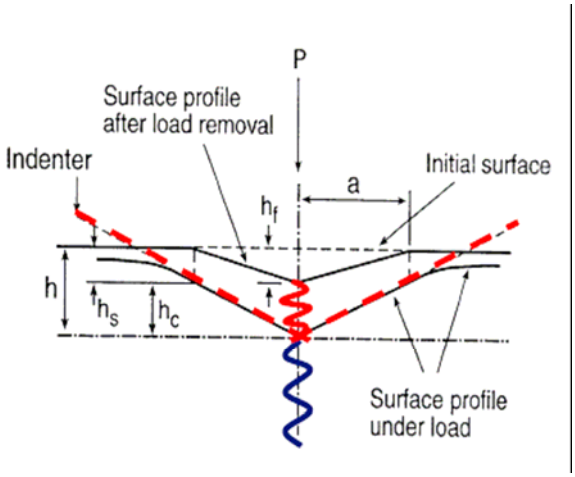


**Figure 13: Schematic of displacements observed during an indentation experiment (after Oliver and Pharr [37] – see also [35])**

Instrumented nanoindentation may be used to determine the stiffness of contact, and therefore indentation modulus $\mathbf{E_{IT}}$ and indentation hardness $\mathbf{H_{IT}}$ (equivalent to Meyer Hardness and similar to HV for a Vickers indenter) and the Martens hardness HM (previously known as Universal hardness, HU) of a material [35]. The HM value is calculated by dividing the test force **P** by the surface area of the indenter penetrating beyond the original surface of the test piece $\mathbf{A_s(h)}$. The Martens hardness is a combination of elastic and plastic indentation responses, and therefore has no direct correlation either to a physical property such as elastic modulus, or to traditional hardness scales (see [35] for further details).

Time-dependent material properties may also be investigated by measuring the continued displacement under a constant applied force. Fracture toughness properties may also be determined by calculating the ratio of elastic to plastic work done during an indentation. The indentation hardness $\mathbf{H_{IT}}$ is calculated from the test force, **P**, divided by the projected area of the indenter in contact with the test piece at maximum load:

$$\mathbf{H_{IT}} = \frac{\mathbf{P}}{\mathbf{A(h_c)}} \qquad \textbf{(12)}$$

The indentation modulus, $\mathbf{E_{IT}}$, is calculated from the slope of the unloading curve through the formula:

$$\mathbf{E_{IT} = \left(1 - \nu_{IT}^2\right) \Big/ \left\{ \frac{2}{\sqrt{\pi}} \frac{\sqrt{A(h_c)}}{S} - \frac{\left(1 - \nu_{indenter}^2\right)}{E_{indenter}} \right\}} \qquad \textbf{(13)}$$

where $\mathbf{\nu_{IT}}$ and $\mathbf{\nu_{indenter}}$ are the Poisson's ratios of the sample and indenter respectively, **S** is stiffness, and $\mathbf{h_c}$ is the contact depth value, which is dependent on the shape of the indenter. Power law or splines fitting routines are used to determine the slopes of the high portion of the unloading curves (Figure 12). For homogeneous and isotropic materials, $\mathbf{E_{IT}}$ approaches the Young's modulus of the material.

A wide range of indenter geometries is available including cube corner, Knoop or ball indenters, Berkovich and diamond sphero-conical indenters. Berkovich is possibly the most popular indenter geometry used with instrumented indentation. Since three facets cannot form a line of conjunction and must meet at a point, this geometry can be used down to very small depths. The most commonly used version of the Berkovich indenter is now the “modified Berkovich” with a facet angle of 65.3°. This angle ensures that the cross sectional area to depth ratio of a modified Berkovich is almost the same as that of a Vickers indenter, thus enabling direct measurement correlation between the two geometries. The cube corner geometry, which is used for indenting very thin coatings and generating cracks, is a three-sided indenter with a much higher aspect ratio (lower opening angle) than the Berkovich. At very shallow depths its main advantage is an ability to support a tip with a very small radius of curvature. This geometry concentrates the force into a smaller indent area, and thus higher energies can be generated. The literature suggests that this geometry is more difficult to calibrate and may exhibit an indentation response that deviates from the standard contact mechanics employed in BS EN ISO 14577-2. Corner cube indenters are more fragile than other geometries and have a tendency to wear more rapidly [35].

The resultant contact area, and hence penetration depth is dependent on the surface roughness of the sample. For the same contact area, indentation depth is higher for a roughness peak compared to an ideal plane horizontal surface, which is higher than for a roughness valley. In order to exclude (or minimise) the effect of surface roughness, which can be significant, it is advisable to carry out an appropriate number of tests commensurate with the magnitude of surface roughness (i.e. scatter increases with increasing surface roughness). An average of 15-25 tests should ensure a reasonable representation of surface properties [40].

There are a number of uncertainties associated with nanoindentation measurements in addition to surface roughness, and “pile-up” and “sink-in” of material around the tip-sample contact previously mentioned. Sources of measurement uncertainty include: load frame compliance, detection of a true zero and measurement errors in load and displacement, variability of elastic properties of the sample and indenter materials, indenter tip geometry (i.e. deformation and wear) and thermal drift. The area values obtained for real tips corresponding to a given contact depth will be much different to those values expected for an ideal tip geometry; particularly for contact depths less than 100 nm (commonly used for nanoindentation). The point assumed to represent initial contact ($\mathbf{h} = 0$) could in fact correspond to a significant applied load. The actual penetration could also be a significant proportion of the maximum displacement, $\mathbf{h_{max}}$.

The elastic modulus of polymeric materials is known to increase with decreasing indentation depth (often referred to as indentation size effect). The discrepancy may be due to surface effects, but there is no evidence to support the hypothesis that **E** (surface) > **E** (bulk). The most likely cause is indenter tip defects near the tip apex and decreased signal-to-noise ratios at low load and displacement levels. Viscoelastic creep during unloading can dramatically affect the slope of the unloading curve, and hence result in errors in modulus and hardness measurements.

Advantages and disadvantages of nanoindentation are summarised below. Most of the factors that adversely effect nanoindentation measurements can be avoided or at least minimised through good measurement practice (see [35]).

| Advantages | Disadvantages |
|---|---|
| • Straightforward specimen preparation and handling.<br>• Direct method of *in-situ* characterisation of interfacial and interphase properties:<br>  • Hardness,<br>  • Elastic modulus (fibre, matrix, interphase),<br>  • Yield stress,<br>  • True stress/strain curves,<br>  • Interfacial adhesion strength,<br>  • Fracture toughness,<br>  • Strain hardening,<br>  • Surface residual stresses,<br>  • Glass transition temperature,<br>  • Interphase dimensions.<br>• Time-dependent (creep/stress relaxation) behaviour.<br>• Applicable to most fibre-matrix combinations.<br>• Straightforward data analysis. | • Large uncertainty in measured data:<br>  • Load frame compliance correction,<br>  • Calibration errors,<br>  • Difficulty in establishing true zero for load and displacement,<br>  • Variability in indenter tip geometry,<br>  • Wear and deformation of indenter tip,<br>  • "Pile-up" and "sink-in" of material around indentation,<br>  • Variability of elastic properties of the sample and indenter materials.<br>• Surface roughness effects measurements.<br>• Viscoelastic behaviour effects unloading slope.<br>• Thermal drift.<br>• Vibration – need anti-vibration table. |

## 4.8 INFRARED SPECTROSCOPY (IRS)

IRS provides information on molecular structure based on specific frequencies associated with internal vibrations of groups of atoms in molecules using a laser in the infrared region to excite the target material and analyse the frequencies absorbed. It makes use of the fact that for polymeric materials the chemical bonds between the atoms in the polymer molecules can rotate or vibrate at frequencies in the IR range of the electromagnetic spectrum (i.e. at wave numbers from 100 - 4000 $cm^{-1}$). The resonant frequencies are determined by the shape of the molecular potential energy surfaces, the masses of the atoms and, by the associated vibronic ("vibrational" and "electronic") coupling. It is assumed that vibrational and electronic interactions of a molecule are interrelated and influence each other. In order for a vibrational mode in a molecule to be IR active, it must be associated with changes in the permanent dipole.

IR spectra of a sample is collected by passing a beam of IR light through the sample. Examination of the intensity of transmitted radiation reveals the quantity of energy absorbed at each wavelength. This can be achieved with a monochromatic beam (continuous wave), which changes in wavelength over time, or by using a Fourier Transform Infrared (FTIR) spectrometer to measure all wavelengths simultaneously. From this, a transmittance or absorbance spectrum can be produced, showing at which IR wavelengths the sample absorbs radiation. At certain resonant frequencies characteristic of the specific sample, the radiation will be absorbed resulting in a series of peaks in the spectrum.

The Fourier transform is a mathematical technique for determining these characteristic frequencies from a single composite signal. Analysis of these absorption characteristics reveals details about the molecular structure of the sample. IRS works almost exclusively on samples with covalent bonds. The more complex the molecular structure the more absorption bands (i.e increase complexity of the spectra). The technique can be used to analyse gases, liquids and solids. Both qualitative and quantitative chemical analysis data can be obtained. It is a key tool for assessing polymer chemistry (e.g. monitoring state of cure).

Recent developments include pulsed FTIR, which produces a similar spectrum as a conventional spectrometer, but in a much shorter time. Instead of varying the energy of the electromagnetic radiation, FT spectroscopy exposes the sample to a single pulse of radiation and measures the response. The resulting signal, called free induction decay, is a direct measurement of the temporal coherence of the light and contains a rapidly decaying composite of the characteristic frequencies for that sample.

There are two major methods for preparing solid samples for FTIR both of which are destructive and result in slight differences in spectra due to differences in the physical state of each sample.

- Crushing the sample with a mulling agent (usually nujol) in a marble or agate mortar, with a pestle and then a thin film of the mull is applied onto salt plates and measured; and

- Grinding a quantity of the sample with a specially purified salt (usually potassium bromide) finely (to remove scattering effects from large crystals). The powder mixture is then crushed in a mechanical die press to form a translucent pellet through which the laser beam of the spectrometer can pass.

Polymeric materials can be prepared using the cast film technique. The sample is first dissolved in suitable, non-hygroscopic solvent. A drop of this solution is deposited on surface of potassium bromide or sodium chloride cell. The solution is then evaporated to ensure specimen is completely dry and the film formed on the cell is analysed directly. Care should be taken to ensure that the film is not too thick otherwise light cannot pass through. This technique is suitable for qualitative analysis.

## 4.9 DIELECTRICS

In this technique, electrodes are applied to the sample to monitor the intrinsic electrical properties of the material (i.e. measurement of voltage and current changes between the electrodes). The application of the electric field can produce two effects.

- It may cause the charges within the material to flow (i.e. electric current); on removal of the electric field the flow of charge ceases (and not reversed); or

- It may produce field changes in the relative positions of the electric charges resulting in electric displacement of the charges, which is completely reversed on removal of the electric field. A material exhibiting this behaviour is called a dielectric (e.g. polymers).

**Basic principle of dielectric measurements:** The application of a sinusoidal voltage to a pair of electrodes creates a localised electric field to be generated across the material. This induces ion motion and dipole rotation within the material generating a sinusoidal current. In the case of polymeric systems, these motions are hindered by viscous drag, resulting in a phase difference between the applied voltage and the stimulated current, as shown in Figure 14 (see [41]). Charge redistribution and reorientation only occurs if the charged species are sufficiently mobile to respond within the timescale/frequency of the excitation field.

The dielectric behaviour of polymeric materials in an oscillating electrical field is completely similar to dynamic-mechanical behaviour under alternating stresses (see [42–43]). In both cases, the delay is expressed as a loss (or phase) angle **δ**. The term used to relate the ratio of electric energy loss to energy stored is the dimensionless parameter **tan δ**, known as the loss tangent (or dissipation factor).

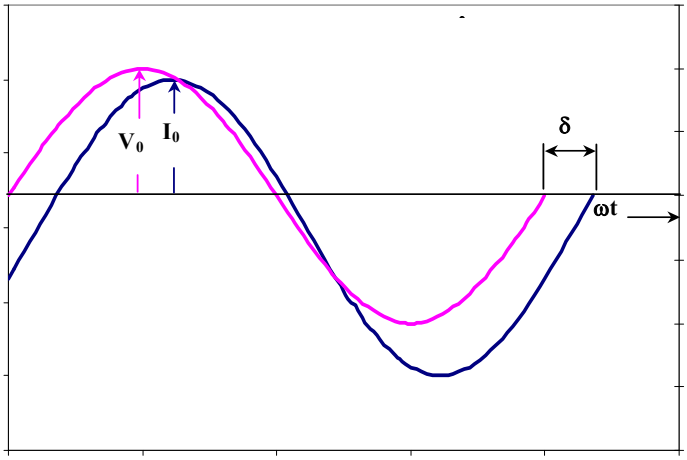


**Figure 14: Out-of-phase response between applied voltage and current**

Dielectric information may be presented in a number of equivalent ways [44-45]. The general approach is to measure the dielectric constant (permittivity, electric inductive capacity) of the material. Permittivity ε may be expressed as a complex quantity [44]:

$$\varepsilon^* = \varepsilon' - i\varepsilon'' \qquad \textbf{(14)}$$

where **ε′** is the real part (dielectric constant or electric inductive capacity) and the imaginary **ε′′** part (dielectric absorption or loss factor). The loss tangent **tan δ** is related to **ε′** and **ε′′** by the following relationship [44]:

$$\tan\delta = \frac{\varepsilon''}{\varepsilon'} \qquad \textbf{(15)}$$

The parameters **ε** and **δ** are generally measured over a wide frequency **ω** range varying from $10^{-4}$ to $10^{11}$ Hz. Alternatively, **ε′** and **ε′′** can be expressed in terms of impedance **Z** (complex variable) [41, 46]:

$$\varepsilon' = -\frac{Z''}{\omega C_0 Z^2} \quad \text{and} \quad \varepsilon'' = -\frac{Z'}{\omega C_0 Z^2} \qquad \textbf{(16)}$$

$$\mathbf{Z = Z' - iZ''} \tag{17}$$

$$|\mathbf{Z}| = \sqrt{(\mathbf{Z'})^2 + (\mathbf{Z''})^2} = \frac{\mathbf{V_0}}{\mathbf{I_0}} \quad \textbf{and} \quad \frac{\mathbf{Z''}}{\mathbf{Z'}} = \tan\delta \tag{18}$$

$\mathbf{C_0} = \boldsymbol{\varepsilon_0}\ \mathbf{A/d}$ is the vacuum geometric inter-electrode capacitance of the cell; $\boldsymbol{\varepsilon_0}$ is permittivity of free space ($8.854 \times 10^{-12}$ $Fm^{-1}$), **A** is area of capacitance and **d** is electrode spacing of the cell (**A/d** is a constant).

The data may be presented in a number of forms including plots of real and imaginary components as a function of frequency either in logarithmic or linear form. Dielectric functions are often power-law functions of frequency and are best presented in log-log form. Alternatively, polar plots of the imaginary component against real component as linear or logarithmic presentation are used.

The analysis used in the interpretation of dielectric data depends on the material state (i.e. liquid or solid). In most general terms, it is possible to distinguish two fundamentally different types of dielectric responses described by the generic terms 'dipolar' and "ionic' (or 'charge carrier') behaviour [45]. Dipolar polarisation leaves a zero residual field on discharging, whereas charge carriers produce partial recovery on discharge, but leaves a finite residual polarisation in the system. The relaxation time constant, $\boldsymbol{\tau}$, defines the polarisation decay time upon removal of the exciting field and is a fundamental material property.

- Dipolar component - dominates at high frequency and high viscosity. In dipolar materials, such as polymers undergoing glass-to-crystalline transition, there are fundamental differences between the responses above and below the glass-transition temperature $\mathbf{T_g}$. Below $\mathbf{T_g}$ the loss peaks are broader.

- Ionic component - dominates at low frequency and low viscosity. At sufficiently high temperatures, all materials tend to show increasing movement of ions, either intrinsic to the lattice in ionic solids, or extrinsic due to impurities in purely covalent lattices (including many polymers). This can be expected to normally lead to direct current (dc) conduction.

Many materials do no not simply fall into one or the other of the above categories, but may display both relaxation and conduction behaviour. Modelling dielectric response is further complicated by additional factors, such as electrode polarisation - accumulation of ions at the polymer-electrode interface, and interfacial or space charge polarisation - accumulation of charges at boundaries in heterogeneous systems. Electronic polarisation (displacement of electrons in an atom from equilibrium) and atomic polarisation (deflection of atoms in a molecule from equilibrium) in the presence of an electric field are considered instantaneous effects, forming the minimum background polarisation levels due to an applied field in the frequency range $10^{-4}$ to $10^{11}$ Hz.

There are several electrode configurations available, as shown in Figure 15. The two principal types are [41]:

- **Inter-digitated sensors** are single surface, comb-like metallic electrode patterns printed onto a small, thin insulating substrate layer. These devices produce localised fringing fields, between adjacent electrode fingers of opposite polarity, extending out into the resin to a distance determined by the electrode geometry/spacing.

- **Parallel plate (bulk) sensor pairs** are solid areas of metallic electrode deposited onto an insulating base. These produce a uniform electric field between the plates of opposite polarity.

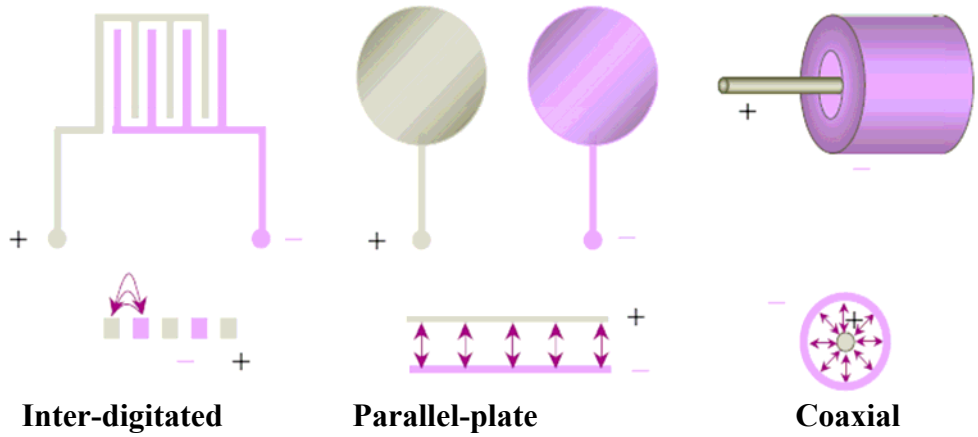


**Figure 15: Basic dielectric sensors and resultant electric fields [41]**

Dielectric sensors can be either implanted or reusable, and positioned externally for surface or embedded for internal measurements. Sensors need to be protected from the possibility of electric short-circuiting against any conductive components within the material (metallic particulate fillers or carbon fibre reinforcement), but must still remain in intimate contact with the resin during processing. Usually a thin layer of glass-fibre fabric, polyimide film or thin porous polytetrafluoroethylene (PTFE) peel ply is sufficient to protect electrodes from short-circuiting. It is important to ensure good contact between the sensor and sample surface. Alignment and separation of the electrodes must be tightly controlled to ensure valid results. The impedance frequency sweep time must be short enough to ensure that changes in dielectric properties are minimal during the measurement and can be considered instantaneous (e.g. cure monitoring of an adhesive). The sensors are connected to an impedance analyser, which is used to perform the electrical measurements.

Recent developments have resulted in the emergence of improved electric insulants based on nanoparticulate reinforced thermosetting resins and polyolefins when compared with conventional (micron-sized particulates) [15]. These improvements appear to be closely related to the control of internal charges in the bulk resin, which stem from increased interfacial surface area and interfacial bond strength. The degree of dispersion of the nanoparticles is pivotal in determining the dielectric behaviour. Clustering (particle agglomeration) can be expected to result in local modifications of the electrical conductivity and admittance (i.e. $\mathbf{Y(\omega) = 1/Z(\omega)}$).

Wu and Kong [47] showed that complex permittivity spectra for multi-walled carbon nanotube reinforced epoxy composites were strongly dependent on the filler content. A distinct resonance peak was observed at ~1.5 GHz for nanocomposites with high filler content. The peak shifted downwards as the filler content increased. Tjong et al [48] observed that the electrical properties of multi-walled carbon nanotube reinforced polypropylene nanocomposites were highly dependent on the content and dispersion of carbon nanotube reinforcement. The dielectric constant and conductivity of PNCs have also been observed to decrease following material deformation [49] and were sensitive to changes in frequency and temperature [50]. Emphasising the need for accurate control of test conditions.

In order to determine the dielectric characteristics of PNCs, it is recommended using a low voltage dielectric analyzer (DEA) with a bandwidth 50 Hz to 20 kHz. The DEA should be capable of operating over the frequency range $10^{-4}$ Hz to 20 GHz, or higher. It is recommended to use a pulse generator with a 5 ns pulse width. Tapered dielectric waveguide probes are capable of mapping the spatially varying dielectric properties of materials with a spatial resolution of better than 500 μm at a frequency of 150 GHz. Typical specimen dimensions are 12-13 mm in diameter and 0.5 to 1 mm thick.

## 4.10 ELECTRICAL IMPEDANCE TOMOGRAPHY (EIT)

EIT is a technique in which an image of the conductivity or permittivity of a component is inferred from surface electrical measurements. Conducting electrodes are attached to the surface of the sample and small alternating currents applied to some or all of the electrodes. The resulting electrical potentials are measured, and the process repeated for numerous different configurations of applied current. The electrodes are positioned with equal spacing around the object to be imaged, thus defining a plane through the object. Voltage profiles are collected for all drive and receive electrode-pair combinations, and images are reconstructed as though the data was obtained from a 2-D object when in practice objects are three-dimensional. An N-electrode system provides N(N-1)/2 independent measurements.

2-D images show that there are significant contributions to the image from off-plane conductivity changes. This means that, unlike 3-D X-ray images, which can be constructed from a set of independent 2-D images, for 3-D EIT it is necessary to reconstruct images from data collected over the entire surface of the sample volume. If high frequency AC currents are used, the skin effect will cause the current to be transported only through a thin layer immediately below the surface.

**Electrical Capacitance Tomography (ECT)** is a close relative of EIT used for determination of the dielectric permittivity distribution in the interior of an object from external capacitance measurements. The electrodes, which are metallic plates, must be sufficiently large to give a measureable change in capacitance. This means that a limited number of electrodes can be used (typically 8-12). Therefore the technique is limited to producing very low-resolution images of approximate slices. However, ECT is fast, and relatively inexpensive.

## 4.11 EDDY CURRENT

Eddy current testing is routinely used in the aerospace industry (airframe inspection), and to a lesser degree in the automotive, marine and manufacturing industries for detecting cracks and subsurface damage, such as corrosion in bonded structures. The electromagnetic technique can only be used on conductive materials. Flaw size and material variations (e.g. thickness) can be determined using the eddy currents. The technique consists of an energising coil, through which AC current flows, for inducing currents into the metal component. The magnetic field of the coil when in close proximity to a conducting surface will induce circulating (eddy) currents in the surface.

The magnitude and phase of the eddy currents will affect the loading on the coil, and thus its impedance. The presence of variations in material conductivity will either interrupt or reduce the eddy current flow, thus decreasing the loading on the coil and increasing its effective impedance. Changes in voltage are measured and displayed in a manner that indicates the material condition.

The conductivity and permeability (ease of magnetisation) of a material will have a direct effect on the eddy current flow. Eddy current increases with increasing conductivity. Conductivity is often measured by an eddy current technique. The eddy current density, and thus the strength of the response from a flaw, is greatest on the surface of the metal being tested and decreases with depth. Probes can be designed to fit the geometry of the component to be inspected. Penetration depths of 10 mm are achievable on metallic materials (e.g. aluminium) using low frequency eddy probe currents, thus enabling detection of subsurface inclusions, which is invisible from the surface, or thinning of any of subsurface layers.

Since the eddy currents are detected as a change in the complex impedance of the energising coil, which is moved over the surface of the material, it is important that the probe-surface distance is maintained very nearly constant. Where surfaces are rough, the eddy current technique may give rise to the detection of false faults. Suitable material preparation through controlled grinding of the surface may be required prior to eddy current inspection

## 4.12 ULTRASONIC TECHNIQUES

Ultrasonic techniques (e.g. time-of-flight – see Figure 16) may be used to establish relationships between changes in the characteristics of propagating ultrasound and the real-time mechanical properties. The longitudinal velocity, $\mathbf{V_l}$, of a sound wave is directly related to the longitudinal elastic modulus (stiffness), $\mathbf{E_1}$, and density, $\boldsymbol{\rho}$, of the material, through the relationship:

$$\mathbf{E_1 = \rho V_l^2} \qquad \textbf{(19)}$$

By using probes that emit and detect ultrasound changes in modulus can be detected, which then provide information on the state of a material, such as the viscosity and hence state-of-cure of resin systems [51].

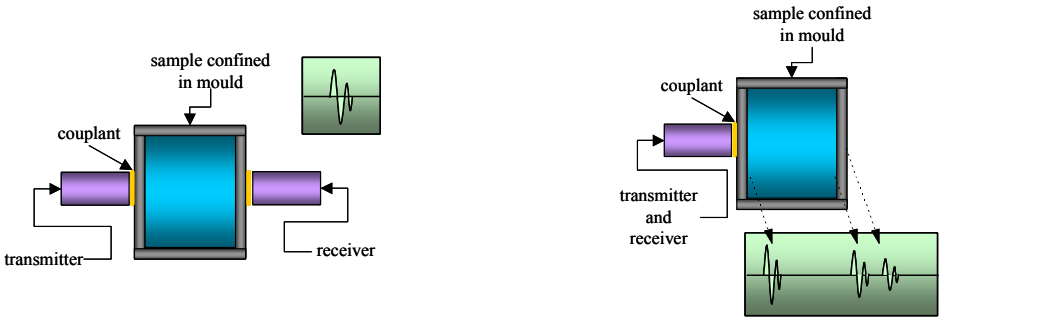


**Through-transmission mode**
**(inset – received signal)**

**Pulse-echo mode**
**(inset – received signal + signals from mould walls)**

**Figure 16: Time-of Flight [51]**

It is also possible to determine information about the viscoelastic properties of the matrix by monitoring the attenuation of the ultrasound signal. The attenuation of the ultrasound is at a maximum when losses due to viscous effects in the polymer are at a maximum, and this coincides with $\mathbf{T_g}$.

**Elastic Property Measurements:** Ultrasonic techniques offer an alternative to the conventional mechanical test method for the determination of elastic properties, although its use for characterisation of composite materials has been limited [52-54]. Many of the difficulties encountered in mechanical testing, particularly for evaluating through-thickness properties, are obviated by the ultrasonic pulse method since the applied stress is negligibly small, and a high sensitivity can be obtained on small, thin specimens. Two methods are available for the ultrasonic determination of elastic properties: contact and immersion. The immersion method allows a full set of elastic properties to be determined for a single specimen (80 mm x 20 mm x 5 mm). The material under investigation is immersed in a liquid, which acts as an ultrasonic couplant. In order to obtain all the stiffness components, the sample is placed on a turntable to facilitate wave propagation in the required directions (Figure 17).

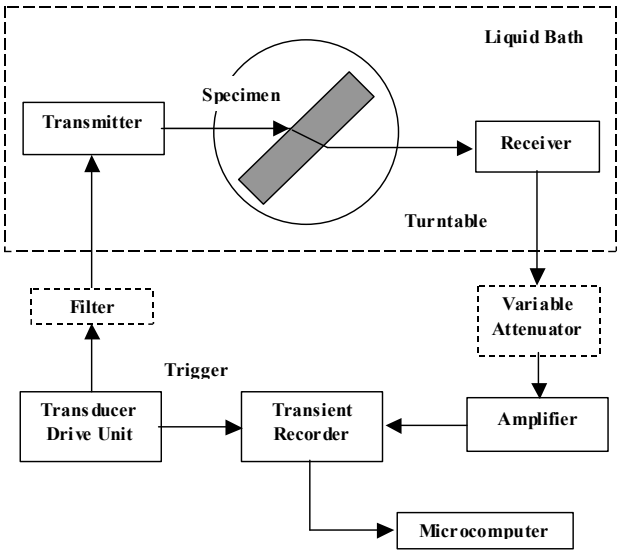


**Figure 17: Schematic representation of the immersion equipment**

Alternatively, the contact method requires several small specimens and a transducer-coupling medium to be used. This method requires that both the transmitting and receiving ultrasonic transducers be attached directly to the specimen, on opposing faces, with the aid of the coupling medium (water-based gel). The electronic equipment required is identical to that employed for the immersion method. Since all the stiffness components of an orthotropic material cannot be deduced from a single specimen, several small specimens need to be cut to allow wave propagation in known planes and directions. Only small amounts of material are required for the tests, at high frequencies, a parallel beam of ultrasound may be propagated with a small cross-sectional area (typically a 5 MHz transducer can produce a plane wave 10 mm across). Ultrasonic transducer frequencies employed are typically between 0.1 and 10 MHz.

In the vicinity of a surface, the wave velocity is lower than that in the bulk material. This causes a change in the shape of the pulse, introducing an error into the velocity measurement. It is therefore necessary to use a wavelength, which is sufficiently small compared with the dimensions of the sample to ensure true plane wave conditions exist. This condition is satisfied when sample dimensions are greater than a few wavelengths. Other factors that can directly influence the accuracy and consistency of results include angle measurements (see Figure 17), sample density and homogeneity, sample dimensions, temperature and surface finish (tolerance of ±0.01 mm, or better). The wave velocity in water varies with temperature. Discrepancies in the wave velocity measurements alter the stiffness matrix constants and, consequently, the engineering properties that are computed using these values. Small aberrations in velocity measurements can lead to dramatic changes in stiffness components. This occurs as a result of the dependence of these parameters on other stiffness components. A detailed description of the theory behind the technique can be obtained from references [52-54].

Unpublished work conducted at NPL has shown that accurate results can be achieved on good quality materials. Composite materials tested included unidirectional carbon-fibre/epoxy and glass-fibre/epoxy, and glass-fibre fabric/epoxy. The elastic modulus values agreed with both theoretical predictions, based on measured volume fractions and manufacturer's fibre and matrix property data, and with the mechanical test results. Shear moduli tended to be higher than both predictions and mechanical test values. This was expected as the non-linear, matrix dominated response of the material was being observed at high frequency and low strain. The Poisson's ratio values were the least accurate or consistent results, however, this is inherent with both ultrasonic measurements and mechanical testing.

**Ultrasonic Resonance Spectroscopy:** The basic principle of operation of ultrasonic resonance spectroscopy is similar to other ultrasonic techniques previously discussed. A continuous sine wave excitation of constant amplitude is used to drive an ultrasonic transducer in contact with the sample surface. The sample is forced into mechanical resonance. The response of the sample is detected using a receiver at a second location on the surface. Both the amplitude and the relative phase of the received signal are recorded over a range of discreet test frequencies so that spectra of amplitude and phase are recorded. Typical test frequencies ranging from 100 Hz to 10 MHz, and higher are employed. The technique can be used to inspect an entire component in a single test, thus enabling rapid inspection suitable for production environments.

Acoustic parameters, such as velocity and attenuation, are linked to the viscoelasticity and microstructure of the propagation medium [55]. The acoustic parameters can be measured by means of pulsed ultrasonic spectroscopy. It is possible to relate changes in ultrasonic properties to moisture content and the level of material degradation (matrix cracks), and also identify damage mechanisms. Changes in frequency dependency of velocity and attenuation have been related to matrix cracking. The length of the ultrasonic pulse and the size of the sample limit the resolution of this technique. Ultrasonic resonance spectroscopy combined with spectra analysis and neural network techniques is an attractive tool for quality assessment purposes.

**Scanning Acoustic Microscopy (SAM):** This NDE technique consists in immersing the test sample in a liquid coupling medium, and then focussing ultrasonic waves on it and detecting either the transmitted or reflected pulses. The simplest case is pulse-echo mode with a single ultrasonic transducer emitting and receiving the ultrasonic beam. When the detector is mounted on a 2 or 3 dimensional scanning head it can be moved around to map out areas of interest, and so form an image. The test sample must be amenable to being immersed in liquid (normally water) to facilitate ultrasound coupling between the ultrasonic transducer and the sample.

The maximum resolution depends on the Raleigh limit of the wavelength (frequency) used, but SAM systems are available with spatial resolution of 20 μm. SAM utilizes very high frequency (typically 5 to 75 MHz) ultrasound to inspect materials. Higher frequencies provide better resolution, but lower frequencies achieve greater penetration into the material. The near-field acoustic microscope was developed to overcome the Raleigh resolution limit. The principle behind this kind of microscope consists of producing an acoustic wave in a tiny area just in the vicinity of the surface (near-field area) through different interaction mechanisms and by detecting this acoustic wave, the acoustic properties of materials are obtained at a high resolution, which is independent of wavelength.

The ultrasonic beam is focused using lenses to a specific range of depth in the test sample. Since ultrasonic transducers have depth of field, the entire sample may be in focus on thinner parts. The ultrasonic signal is a short pulse that travels through the material being tested. It is reflected back to the transducer when it strikes interfaces within the material. The transmitted sound waves that are reflected back arrive back at the transducer at different times, which correspond to different depths in the material. High spatial (lateral) resolution of the order of 1-2 μm can be achieved through the use of high frequency transducers (i.e. 200 - 600 MHz), although signal-to-noise ratio decreases with increasing frequency. SAM has been used to detect surface cracks in soda lime glass and MgO single crystals with a depth as small as 25 μm, even though there is a dead zone of some 10-15 μm.

**Scanning Near-Field Acoustic Microscopy (SNAM)** is method for imaging the topography of non-conducting surfaces with a potential lateral resolution in the sub-micron range. The basic element of this method is a distance sensor consisting of a sharply pointed vibrating tip, which is part of a high-Q (gain) quartz resonator driven at its resonance frequency. The decrease in resonance frequency or of the amplitude of vibration when an object comes into the proximity of the tip serves as the key signal.

The dependence of this signal on pressure and composition of the coupling gas shows that the hydrodynamic forces in the gas are responsible for the coupling between samples and probe tip. The sensor is incorporated into a scanning device. Well-resolved line scans have been achieved for a grating of 8 μm periodicity with lateral resolution of 3 μm and a vertical resolution of 5 nm.

**Laser-Ultrasonics (or Laser-Ultrasound)** is a non-contact technique that uses lasers to generate and detect ultrasonic waves. It is used to measure material thickness, detect flaws and materials characterisation [56-57]. A laser-ultrasonic system consists of a generation laser, detection laser and detector. Ultrasonic waves are generated using a pulsed laser (typically a few nanoseconds of duration with an energy less than one joule). Solid state Q-Switched Nd:YAG and gas lasers ($CO_2$ or Excimers) are used to generate the laser pulse. Detection lasers are continuous or long pulse (~10-20 ms) with a long coherence length. The detection laser light reflected (or scattered) by the material surface is perturbed (e.g. Doppler effect) by the arrival of ultrasonic waves. The perturbation is usually detected using interferometric techniques, such as confocal Fabry-Perot or photorefractive interferometers, which demodulate the detection light. Prototype versions using remote sensors have been used in the hostile (high temperature) environment of steel production.

New developments include scanning probe systems that combine AFM with scanning acoustic microscopy enabling simultaneous imaging of sample topography and monitoring of ultrasonic surface vibrations in the MHz range. For detection of the distribution of the ultrasonic vibration amplitude, a part of the position-sensing light beam reflected from the cantilever is directed to an external knife-edge detector (see AFM). Acoustic images with a lateral resolution of about 100 nm suitable for inspecting nanocomposites have been achieved at an ultrasonic frequency of 20 MHz.

## 4.13 OPTICAL TECHNIQUES

This section evaluates optical techniques that may be used either directly or indirectly to measure the degree of dispersion of particles in fluids and solids.

**Photon Correlation Spectroscopy (PCS) (or Dynamic Light Scattering (DLS)):** In this technique, the Brownian motion (movement in random direction) of sub-micron particles is measured as a function of time. A low power (10 – 40 mW) laser beam is diffracted by particles in suspension. He-Ne or argon ion lasers, or more recently diode lasers are used to provide the light source (high stability and long coherence length). Diode lasers offer a number of advantages including low cost, miniaturisation, ruggedness and fibre optics compatibility. The diffusion of particles causes rapid fluctuations in scattering intensity around a mean value at a certain angle (varying from 10 to 150°). The relative positions of the particles in the scattering volume at any instant in time, determines the degree of constructive or destructive interference of scattered light at the detector. Since the velocity of the particles is dependent on the particle size, information about size is contained in the rate of fluctuation of scattered-light intensity. The particles have a different refractive index than the surrounding medium, and are stable during the measurement. The fluctuation of scattered light from particulates in a liquid medium is recorded and analysed, either in the frequency domain or in the correlation delay time domain depending on the application [58].

The detected scattering may be directly from individual particles (single scattering), or from multiple scattering in the case of concentrated solutions or suspensions. The calculated correlation function results in a diffusion coefficient for a given temperature and viscosity, which can be converted to particle size. The sample cell is usually a simple square or round cuvette with the sample size of a few millilitres. Particles in the scattering volume, which is the cross-section between the light beam and the detecting optics, scatter light in all directions. The scattered light is collected at the scattering angle, either by an aperture lens set-up or by an optical fibre, and then detected by either a low-noise photo-multiplier tube or an avalanche photodiode. The electric pulses are amplified, stretched and fed into an autocorrelator to compute the intensity autocorrelation function (duration of short pulses - see [58]). The lower particle-size measurement limit (1-2 nm) is determined by the scattering intensity and experimental noise (e.g. temperature fluctuations and electronic noise). The upper particle-size measurement limit (1-5 μm) is primarily determined by the sedimentation rate. It is also is dependent on material density and dispersant viscosity.

A measurement at a single scattering angle is often inadequate because particles of different sizes have different scattering intensities and different decay constants at a given scattering angle. The decay constant is inversely proportional to the hydrodynamic diameter of particles. The angular scattering intensity patterns per unit volume for particles of different sizes (masses) are different due to intra-particle destructive interference. The angular scattering pattern for solid spheres can be described by a spherical Bessel function. The pattern is oscillatory having a maximum at the zero scattering-angle followed by a sequence of minima and maxima of decreasing intensity. The larger the particles, the larger the absolute scattering intensity per unit volume will be at small scattering angles (i.e. scattering per unit volume is proportional to the mass of the particle at small scattering angles). The intensity of scattered light decreases significantly with increasing scattering angles; especially for particles smaller than the laser wavelength. The shape of the angular pattern becomes smoother and less angle-dependent as particles become smaller.

The signal detected is weighted by the scattering intensity of the constituents of the sample and not by the volume or weight percentages of the constituents. Measurements at small scattering angles are heavily weighted by the scattering from the larger particles in the sample. Conversely, measurements at large scattering angles are heavily weighted by the scattering from the smaller particles in the sample. Errors in size distribution will result from single-angle measurements due to different scattering intensities from particles of different sizes. Multi-angle measurements are recommended to eliminate the blind spot effect and to verify size distribution. For solid particles, the mass changes as the cube of the diameter change.

PCS is suitable for measuring mean particle size and particle size distribution at the micro- and nanoscale (1 nm – 5 μm), diffusion coefficient ($10^{-3}$ - $10^{-8}$ $mm^2/s$) and molecular weight ($10^3$ - $10^{12}$ g/mol) of polymers in solution. It is commonly used in particle characterisation, and polymer and colloid studies. The technique is suitable for both solid and soft particles. It provides fast, non-intrusive real-time size measurements, and is suitable for on-line quality control of production. The scattering angle range for multi-angle instruments is typically 10° - 150° with a resolution of 0.01°. Sample preparation is relatively straightforward. Temperature control is essential to minimise measurement uncertainties due to temperature fluctuations.

**Laser Diffraction (Static Light Scattering (SLS)):** In this technique, the scattering pattern, obtained from illumination of dispersed particles with a laser beam, contains information relating to particle size and particle size distribution. The interaction between particles and light is mainly dependent on particle size, shape, surface roughness and refractive indices of material and dispersing medium. For a specific material, the scattering pattern of a particle is unique for its size. Deconvolution of the sample scattering pattern with an optical model, such as Mie or Fraunhofer results in the particle size distribution [58]. Many instruments have both static and dynamic light scattering capability.

**Image Analysis and Time of Transition (TOT):** Image analysis uses a CCD video camera microscope to acquire an optimal image of the particles' shape. The technique provides a variety of parameters such as Feret diameter, area, perimeter, shape factor and aspect ratio. The 2-D shape and size information is complemented by a Time of Transition (TOT) laser analysis. Time size mapping provides the particle size distribution. The strength of the TOT theory is that it relates solely and directly to particle size, rather than to secondary properties from which size may be inferred. A laser beam circularly scans the sample measurement volume. As the laser spot individually bisects the particles within the sample volume, interaction signals are generated. Since the beam rotates at a constant speed, the duration of interaction with the individual particles provides direct measurement of the particles' size. The measurements are performed using particle size and shape analyser.

**Raman Spectroscopy** has proven to be a useful technique for characterising carbon-based materials. It is used to study the structural, electronic, vibrational and magnetic properties of carbon nanotubes (CNTs). Providing information on the chemical functionality and dispersion of single-walled and multi-walled nanotubes in nanocomposites [59]. Raman spectroscopy is based on the inelastic scattering of monochromatic light. A laser (e.g. Ar+ or He-Ne) excites the material, which is usually in the visible region of the spectrum. The frequency of scattered light is analysed compared with incident values. The technique is similar to infrared spectroscopy (IRS) in determining the nature of molecular structures and is a complementary technique to IRS when characteristic frequencies are weak or for highly absorbing materials. Raman spectroscopy is sensitive to a material's composition and structure and can distinguish between different structural arrangements of similar atoms. The vibrational spectrum of a material is a function not only of its constituent atoms, but also the spatial arrangement and the strength of bonding between atoms. Samples require minimal preparation, but need to be stable to high intensity light and contain no species that fluoresce when excited by visible radiation.

**Light Transmission or Reflection:** The presence of mineral particles (e.g. organoclay) is known to reduce the transparency and surface gloss of polymeric materials, such as polymethyl methacrylate (PMMA), although the effect is less pronounced for nanocomposites compared with microcomposites with equivalent filler content. A reduction in light transmission of 25% has been observed for UV-cured polyurethane-acrylate containing 5 wt.% organoclay [14]. Similar reductions have been observed for surface gloss. An organoclay content of 1 wt.% produced a 50% reduction in surface gloss in the same polymer [15]. The reduction in gloss was attributed to an increase in surface roughness.

A spectrophotometer is used for measuring the transmittance or absorbance/optical density at different wavelengths. The spectrophotometer exposes a 10 mm diameter circular area on the surface to a light source with a daylight colour spectrum and compares the percentage reflectance or transmittance within the visible spectrum (360 - 750 nm wavelength) to that of reference white and black colour tiles [60-63]. The reflectance or transmittance of the sample is measured at 1 nm wavelength intervals over the spectral range 380 to 780 nm.

## 4.14 THERMAL TECHNIQUES

**Dynamic Mechanical Analysis (DMA)**, also known as **Dynamic Mechanical Thermal Analysis (DMTA)** obtains information about the mechanical properties of a material by applying a sinusoidal load to a specimen and measuring the resultant deformation, whilst the sample is subjected to a controlled temperature programme. This technique (often used in conjunction with differential scanning calorimetry (DSC)) enables the determination of mechanical (storage and loss modulus) and thermal properties of polymeric materials (see Figure 18) over a wide range of temperatures (-150°C to 600°C) and frequencies (0.01 to 200 Hz) by free vibration, and resonant or non-resonant forced vibration methods (ISO 6721 [64]) - see also [65-66].

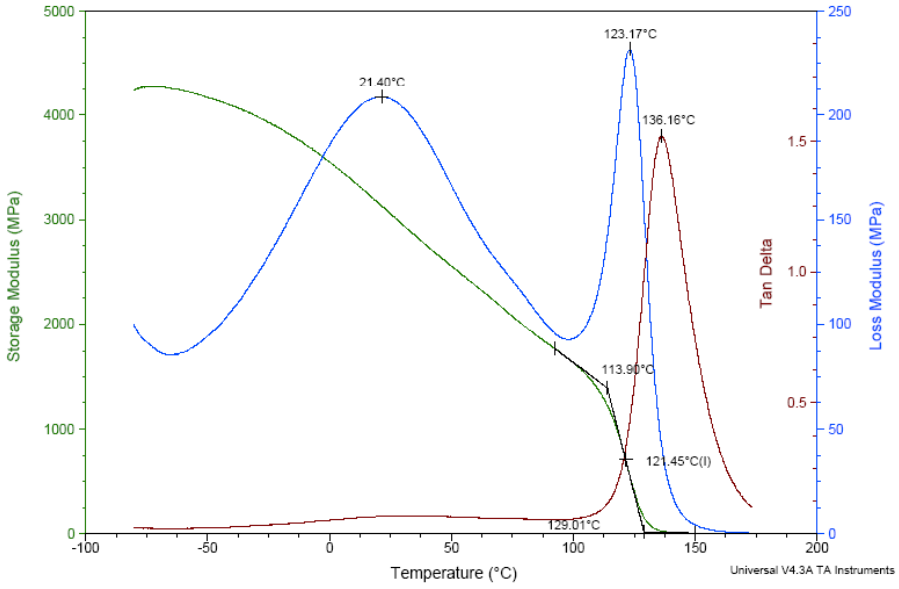


**Figure 18: Typical DMA plot of a clay/polyamide nanocomposite**

Tension, compression and flexure loading configurations can be employed, although flexural samples are generally most popular. Three-point flexure specimens can be up to 50 mm in length, 15 mm wide and 7 mm thick. The sample is mounted on a clamp and then subjected to sinusoidal changes in strain (or stress) while undergoing a change in temperature. DMA is suitable for polymeric materials with stiffness ranging from 1 kPa to 1,000 GPa. DMA can be used to measure heat distortion temperature, and thermal expansion and contraction (i.e. coefficient of thermal expansion (CTE)) under dynamic or isothermal heating conditions. Advantages include fast analysis time (typically 30 minutes), easy sample preparation and wide range of temperature applicability.

**Differential Scanning Calorimetry (DSC)** is used to determine the heat flow associated with material transitions as a function of time and temperature (-60°C to 300°C) or changes in heat capacity using minimal amounts of material. The technique provides quantitative and qualitative data on endothermic (heat absorption) and exothermic (heat evolution) processes of materials during physical transitions caused by phase changes, melting, oxidation and environmental degradation. DSC can be used to measure $\mathbf{T_g}$ and degree of cure. The technique involves slowly heating a small sample of material and measuring the heat absorbed or emitted by the sample as a function of temperature compared to a reference material. DSC can be used to measure changes in $\mathbf{T_g}$ and crystallization behaviour (i.e. crystallization temperature, degree of crystallinity and nucleation rate of spherulites) as a function of filler content for conventional composites and nanocomposites (see Figure 19) [14-15, 68-70]. ISO 11357 [71] specifies methods for thermal analysis of polymeric materials using DSC.

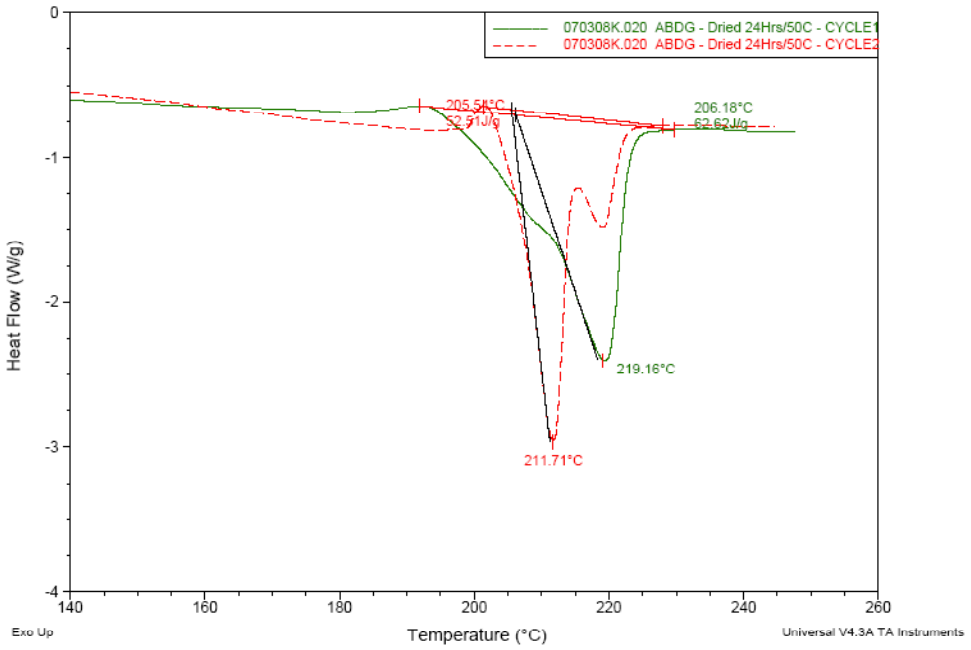


**Figure 19: Typical DSC plot of a clay/polyamide nanocomposite**

The technique has many advantages, including fast analysis time (~30 minutes), easy sample preparation, small test specimens (typically 5-20 mg) and wide range of temperature applicability. A small sample may also be a disadvantage as it may be unrepresentative of the bulk material, particularly if the material is heterogeneous. The sample for testing must also be removed from the manufactured item after the cure has occurred, which means that the test can not be performed in real-time or on-line. For some materials it can be hard to assign a $\mathbf{T_g}$ value, either because the wrong thermal transition has been assigned as the $\mathbf{T_g}$ or because there may be only a small change in heat flux as the $\mathbf{T_g}$ is passed through during the temperature ramp. $\mathbf{T_g}$ can provide semi-quantitative information on the degree of exfoliation of nanoclay particles in nanocomposites [68-70]. Partially exfoliated nanocomposites exhibit higher $\mathbf{T_g}$ values than both the neat polymer and intercalated nanocomposite.

The presence of nanoparticles will alter the crystallization behaviour of thermoplastic polymers [15]. At low loading levels (1–3 wt.%), nanoparticles act as nucleating sites for spherulite formation and accelerate the crystallization rate of the thermoplastic (i.e. activation energy of crystallization of the nanocomposite is lower than the neat polymer). The crystallization rate increases with filler content until a critical value is reached (ca. 5 wt.%). Well-dispersed systems have higher crystallization temperatures than poorly dispersed systems. At higher loading levels (ca. 10 wt.%), the nanoparticles tend to agglomerate and obstruct mobilisation of the polymer molecular chains, retarding crystallization and crystal growth (i.e. activation energy of crystallization of the nanocomposite is higher than the neat polymer).

The degree (or percentage) of crystallinity $\mathbf{X_c}$ can be calculated from the melting heat of crystallization according to the following relationship:

$$\mathbf{X_c(\%) = \frac{\Delta H_m}{(1 - W_f)\Delta H_0} x\ 100} \qquad \textbf{(20)}$$

$\mathbf{\Delta H_m}$ is the melting heat of crystallization of the nanocomposite, $\mathbf{\Delta H_0}$ is the melting heat of crystallization of the 100% crystalline polymer and $\mathbf{W_f}$ is the filler mass fraction.

**Modulated Temperature DSC (MT DSC)** allows the differentiation of overlapping transitions. A sinusoidal modulation is overlaid on the linear heating ramp of the DSC. Depending on the settings, it results in improved resolution and sensitivity not possible using other techniques. Typical reversing events are glass transitions and crystalline melting; and examples of non-reversing events are cold crystallization, evaporation, thermoset cure and decomposition.

**Thermal Gravimetric Analysis (TGA)** can be used to monitor weight changes in a sample as a function of temperature (or time). Its principal uses include measurement of a material's thermal stability and composition. The technique is used for studying degradation processes, providing information on thermal oxidative degradation rates and thermal degradation temperatures of polymeric materials. The technique is not particularly sensitive to the changes in resins due to different states of cure.

**Gel Permeation Chromatography (GPC)** is used to determine several important parameters including average molecular weight and the most fundamental characteristic of a polymer its molecular weight distribution. GPC separates molecules in solution by their "effective size in solution". To prepare a sample for GPC analysis the resin is first dissolved in an appropriate solvent. Inside the gel permeation chromatograph, the dissolved resin is injected into a continually flowing stream of solvent (mobile phase). The mobile phase flows through millions of highly porous, rigid particles (stationary phase) tightly packed together in a column where the size exclusion separation takes place. The pore sizes of these particles are controlled and available in a range of sizes.

A differential refractometer concentration detector (RI) or ultraviolet (UV) detector is used to measure the response to molecular size after separation by the columns. The width of the individual peaks reflects the distribution of the size of molecules for a given resin and its components. The distribution curve is also known as the molecular weight distribution (MWD) curve.

The broader the MWD, the broader the peaks become and vice versa. The higher the average molecular weight, the further along the molecular weight axis the curve shifts and vice versa. The refractive index of polymers is constant above approximately 1000 MW, and thus the RI detector response is directly proportional to concentration. UV absorbance detectors can provide information about composition, while on-line light scattering detectors and viscometers provide information about polymer structure.

Two specialized detectors have been developed with specific applications for GPC. The first is the referenced-flow viscometer detector, which along with the refractometer enables the user to set up a calibration curve, using narrow polymer standards to obtain accurate molecular weights and size. The other detector is the laser light-scattering detector. With the addition of low angle light scattering detection it is the preferred technique for accuracy. The light-scattering detector gives a response proportional to molecular weight and concentration, while the viscometer detector response is proportional to the intrinsic viscosity and concentration. Intrinsic viscosity is inversely proportional to molecular density. Sampling times are typically 30 to 60 minutes.

## 4.15 RHEOLOGICAL METHODS

Rheology is the study of the deformation and flow of matter. The rheological behaviour of polymeric materials is complex and usually comprises of significant viscoelastic behaviour and differing properties in shear and extensional flow fields, characterised by shear viscoelasticity and extensional viscoelasticity [71]. The presence of particles increases the intrinsic viscosity of the fluid. Particle properties that may affect how the filler contributes to the rheology of the mix include [72]:

- Particle shape (and distribution)
- Particle size (and distribution)
- Particle stiffness (e.g. rigid or flexible particles)
- Surface morphology and properties
- Surface chemical properties (surface treatment)
- Interfacial energy (wettability)
- Density (difference between matrix and filler – buoyancy effects)

Flow regimes for viscoelastic fluids can be categorised as shear (where layers of fluid slide past each other) or extensional (where ‘slugs’ of fluid are drawn in tension). Most rheological measurement methods work in shear flow, but some techniques have been developed for extensional flow. A list of methods that have been used to measure the rheological behaviour of filled polymers are listed below (see [14-15, 70-76]):

- Capillary die and slit die extrusion rheometry (ISO 11443 [77])
- Melt flow rate testing
- Rotational rheometry using a wide range of geometries (ISO 3219 [78])
- Oscillatory rheometry (ISO 6721-10 [79])
- Extensional rheometry
- Torque rheometry
- Squeeze flow techniques
- Oscillating probes

The capillary extrusion rheometer and melt flow rate method are used primarily to characterise the shear flow behaviour of polymeric materials. Extensional flow behaviour can be a more sensitive measure of, for example, changes in molecular structure of the material. Alternative techniques not always associated with rheological characterisation, such as ultrasonic or acoustic transmission are also used [72]. The difficulty with ultrasonic and acoustic techniques is relating the properties measured at very high frequencies and low strains to the flow behaviour of the material during processing (equivalent to significantly lower frequencies and higher strains).

Rheological measurements provide correlations between molecular structure and material properties, and between material properties and behaviour in practical situations. These may also be used to predict material behaviour in complex flow situations. This requires sophisticated mathematical treatments using data obtained from simple rheological experiments. It is important to test in the linear elastic region of the material in order to obtain reliable dynamic measurements of the storage modulus $\mathbf{G'(\omega)}$ and loss modulus $\mathbf{G''(\omega)}$ of the complex shear modulus ($\mathbf{G(\omega) = G'(\omega)\sin(\omega t) + G''(\omega)\cos(\omega t)}$) for comparison with other materials [72]. For filled materials it can be difficult, if not impossible, given the operating limits of rheometry instrumentation, to accurately determine the strain limit of the linear viscoelastic region within which reliable, comparable linear viscoelastic $\mathbf{G'}$ and $\mathbf{G''}$ data can be determined.

The filler size distribution effects viscosity, a disperse distribution has a lower viscosity than a less disperse distribution of equivalent volume fraction. Particle clustering (agglomerations) can result in an increase in viscosity and can be induced or destroyed by flow. Particles of sub-micron size are affected strongly by attractive forces. The effects of particle interactions, which are dependent on particle shape, tend to be more significant with high aspect ratio fillers than spherical fillers.

The flow curves (dynamic viscosity $\eta^*$ vs. shear rate (oscillation frequency of the rheometer) $\omega$) obtained under low amplitude oscillatory shear measurement conditions can be fitted using the following power law expression [73-76]:

$$\eta^* = k\omega^n \qquad \textbf{(21)}$$

where **k** is the sample specific pre-exponential factor and **n** is the shear thinning exponent. Shear thinning is a reduction in viscosity with increasing rate of shear in steady flow (the opposite of shear thickening) – see BS 5168 [80].

Parameters **k** and **n** can be directly determined from the logarithmic plot of viscosity $\eta^*$ vs. frequency $\omega$ as below [73]:

$$\log(\eta^*) = \log k + n\log(\omega) \qquad \textbf{(22)}$$

The shear thinning exponent **n**, which is the slope of a straight line fitted to the plot of **log** ($\eta^*$) vs. **log** ($\omega$), is a semi-quantitative measure of nanodispersion (degree of exfoliation) of the sample. In most cases, however, plots of **log** ($\eta^*$) vs. **log** ($\omega$) tend to be curved and **n** is determined by fitting a straight line to the data at the lowest shear rates (~0.01 – 0.1 rad $s^{-1}$). There is no unequivocal relation between the shear thinning exponent **n** and degree of exfoliation (or dispersion).

Measurement of the key characteristics (i.e. shear thinning exponent, elastic plateau at low frequencies and crossover frequencies along with overall pattern of the complex viscosity components **G′(ω)** and **G′′(ω)**) provides valuable information on global exfoliation and the percolation threshold [75-76]. Both the storage and loss moduli for aligned silicate-reinforced PNC samples have been shown to be considerably lower than for unaligned samples [69]. The frequency dependence of both **G′(ω)** and **G′′(ω)** is also much stronger than for aligned samples.

## 4.16 NUCLEAR TECHNIQUES

**Nuclear Magnetic Resonance (NMR)** is a physical phenomenon based upon the magnetic property of an atom's nucleus. All nuclei that contain odd numbers of nucleons and some that contain even numbers of nucleons have an intrinsic magnetic moment. The most often-used nuclei are hydrogen-1 ($^{1}$H) and carbon-13 ($^{13}$C), although certain isotopes of many other elements nuclei (e.g. $^{15}$N, $^{27}$Al and $^{29}$Si) can also be observed, depending on the structure under surveillance [14, 81]. NMR studies a magnetic nucleus, like that of a hydrogen atom (protium being the most receptive isotope at natural abundance), by aligning it with a very powerful external magnetic field and perturbing this alignment using an electromagnetic field (see [81]). The material response to the perturbation field is exploited in NMR spectroscopy and magnetic resonance imaging.

NMR spectroscopy is one of the principal techniques used to obtain physical, chemical, electronic and structural information about a molecule. The resonance frequency absorption bandwidth is inversely proportional to the cube of the nearest neighbour distance. By exploiting this response NMR can be used to study the cure process of thermosetting polymers and probe molecular linkage and orientation of trapped polymer segments within the interlayer spacing of intercalated nanocomposites. The NMR spectral line widths and relaxation times can be used to determine bulk thermal transitions as a function of temperature (i.e. chemical shifts). Relaxation times are dependent on the experimental conditions, such as uniformity of the applied field, shielding due to the bulk material and the time to achieve thermal equilibrium. It has been used to quantitatively determine the degree of clay dispersion in nanocomposites.

**Photon Induced Positron Annihilation (PIPA)** involves penetrating materials with a photon beam. This process creates positrons, which are attracted to nano-sized defects in the material. Eventually, the positrons collide with electrons in the material and are annihilated, releasing energy in the form of gamma rays. The gamma ray energy spectrum creates a distinct and readable signature of the size, quantity and type of defects present in the material.

**Distributed Source Positron Annihilation (DSPA)** uses a positron source emitter to deposit positrons into the subject material. The process is similar to PIPA after the positrons are deposited and attracted to nano-sized defects in the material. PIPA and DSPA technologies detect fatigue, embrittlement, and other forms of structural damage in materials at the atomic level, before cracks appear. PIPA and DSPA can also accurately determine the remaining life of various materials and are more precise than any other existing flaw detection technology on the market.

**Neutron Radiography (NRA)** is an imaging technique, which provides images similar to X-ray radiography. The difference between neutron and X-ray interaction mechanisms produce significantly different and often complementary information. While X-ray attenuation is directly dependent on atomic number, neutrons are efficiently attenuated by only a few specific elements. For example, organic materials or water are clearly visible in neutron radiographs because of their high hydrogen content, while many structural materials such as aluminium or steel are nearly transparent. At the present time, Neutron Radiography is one of the main NDT techniques able to satisfy the quality-control requirements of explosive devices used in aerospace and defence programs.

NRA is a nuclear method that can be used to obtain concentration versus depth distributions for certain target chemical elements in thin solid films. By irradiating the target elements with select projectile nuclei having specific kinetic energies these target elements can undergo a nuclear reaction under resonance conditions for a sharply defined resonance energy. The reaction product is usually a nucleus in an excited state, which immediately decays, emitting ionizing radiation. To obtain depth information the initial kinetic energy of the projectile nucleus (which has to exceed the resonance energy) and its stopping power (energy loss per distance travelled) in the sample has to be known. In order to contribute to the nuclear reaction, the projectile nuclei have to slow down in the sample to reach the resonance energy. Each initial kinetic energy corresponds to a depth in the sample where the reaction occurs (the higher the energy, the deeper the reaction). The energetic emitted $\gamma$ ray is characteristic of the reaction and the number of $\gamma$ rays detected at any incident energy is proportional to the concentration at the respective depth of hydrogen in the sample.

NRA analysis can be used to directly measure localised moisture content through the thickness of polymeric materials. Specimens are conditioned in $D_2O$ instead of $H_2O$ and the resultant deuterium concentrations in the specimen are measured. The surface is bombarded with a finely collimated $^3He$ beam, which reacts with the deuterium in the sample, releasing high-energy protons. The proton yield is directly proportional to deuterium in the reaction volume. Moisture profiles with a resolution of 12 $\mu$m have been measured.

## 5 MODELLING NANOCOMPOSITES

The ideal approach to modelling composite behaviour is to commence with the basic properties of the constituent materials (i.e. filler and matrix) and be able to predict the mechanical behaviour (i.e. elastic and strength properties) of the composite. In modelling composite properties, gross simplifications (i.e. perfect fibre/matrix interfacial bonding and uniformity of matrix properties surrounding the filler) are made in relation to the stress state arising at the interface. Most composite models make no allowance for the influence of interfacial or interphase properties on composite behaviour, but assume perfect bonding between the reinforcement and surrounding matrix. The success of models that exclude these effects is dependent on the quality of the interfacial fibre/matrix bond and environmental test conditions with predictive reliability decreasing for poor quality material and hostile environments.

When the fibres are strongly bonded to the matrix the elastic properties and to a lesser degree the strength properties of conventional composites (including discontinuous reinforced systems) can be calculated using micromechanical models (e.g. Halpin-Tsai and Mori-Tanaka). A key question arises as to whether micromechanical models used to predict lamina properties of conventional composites could also be applied to nanocomposites. Chemical and physical interactions between reinforcing particles and the surrounding polymer and between reinforcing particles themselves can be expected to have a significant effect on material behaviour of nanocomposites resulting in substantially different properties from conventional composites. It is important to account for the intrinsic hierarchical morphology of the dispersed phase (i.e. surface area, interlayer spacing, gallery spacing and platelet thickness – see Figure 20) [15].


**Figure 20: Schematic of layered nanocomposite**

There are two main approaches for modelling nanocomposites: continuum models based on micromechanics used to analyse the global properties of the nanocomposites at the micro- or macro-scale and molecular modelling used to analyse the local load transfers, interface properties or failure modes at the nanoscale. This section examines both micromechanics and nanomechanic models (including molecular dynamics) for analysis of elastic and strength properties of nanocomposite systems. The models considered cover a wide range of length scales from the nanoscale ($10^{-10}$ m) to the macroscale ($10^{0}$ m).

## 5.1 CONTINUM BASED-MODELLING

Continuum-based methods assume the existence of continuum for all calculations and generally don't include the chemical interactions between constituent phases. The continuum-based techniques primarily include computational methods, such as finite element and boundary element methods, and the micromechanics approaches developed for conventional composites.

### 5.1.1 Micromechanics Approach

In nanocomposites the structure of the filler (e.g. a nanotube) can be taken into account, and the properties of an effective fibre can be defined. This can then be used to determine the elastic properties of a composite using a micromechanics approach. Micromechanics approaches typically assume perfect adhesion (perfect load transfer) and ignore interfacial phenomena.

Halpin-Tsai semi-empirical relationships have been used extensively for determining engineering properties of continuous and discontinuous fibre-reinforced systems. The following generalised form can be used to determine the tensile modulus $\mathbf{E_c}$ of a composite (see [14-15, 82-89]):

$$\mathbf{E_c = E_m}\left(\frac{\mathbf{1+\xi\chi\phi_f}}{\mathbf{1-\chi\phi_f}}\right) \tag{23}$$

where:

$$\chi = \left(\frac{\mathbf{E_f}}{\mathbf{E_m}} - \mathbf{1}\right) \Big/ \left(\frac{\mathbf{E_f}}{\mathbf{E_m}} + \xi\right) \tag{24}$$

$\mathbf{E_m}$ and $\mathbf{E_f}$ are the associated matrix and filler Young's modulus respectively and $\phi_f$ is the filler volume fraction. The reinforcing parameter (or shape factor) $\xi$ is dependent on particle geometry, orientation and aspect ratio of the particles. The dimensionless quantity $\chi$ may be viewed as the "reduced" properties of the constituents.

The shape factors for platelet-reinforced composites are given by [87]:

$$\begin{aligned} \xi &= \frac{2}{3}\left(\frac{\mathbf{w}}{\mathbf{t}}\right); \quad \mathbf{E_{11}\ or\ E_{22}} \\ \xi &= 2; \quad \mathbf{E_{33}} \end{aligned} \tag{25}$$

where **w/t** is the aspect ratio of platelet width/platelet thickness.

The nature of Equation (23) becomes clearer if rewritten in the following form:

$$\mathbf{E_c} = \frac{\mathbf{E_f}\left(\mathbf{1}+\xi\phi_f\right)+\mathbf{E_f}\left(\xi-\xi\phi_f\right)}{\mathbf{E_f}\left(\mathbf{1}-\phi_f\right)+\mathbf{E_m}\left(\xi+\phi_f\right)} \tag{26}$$

The central tenet of the Halpin-Tsai relationship is that elastic properties $\mathbf{E_c}$ of a composite material must lie somewhere between the extremes of the Voigt upper bound and the Reuss lower bound. Voigt model corresponds to the mechanical analog of "springs in parallel" and the Reuss model is associated with "springs in series". The arbitrary scaling parameter $\xi$ serves to adjust the effective properties between the upper and lower bounds, and can be treated as an adjustable parameter whose value can be obtained from experimental determination of the property of the composite at a specific fibre volume fraction. Values of $\xi$ are obtained by comparing the calculated values obtained using the Halpin-Tsai equations with exact elasticity solutions through a curve fitting exercise.

Alternatively, Mori-Tanaka mean field theory has been used to assess the overall properties, such as the effective stiffness tensor **C*** of a composite [15]. This approach is based on the Elsheby method for estimating the stress state in composites with spherical inhomogeneous inclusions embedded in an infinite foreign matrix (i.e. different stiffness). Eshelby tensors are, in general, not uniform inside the inhomogeneity but are position-dependent and have the property of radial transverse isotropy (see [90-91]).

The effective stiffness tensor **C*** is given by the following relation [15]:

$$\mathbf{C^* = C_1 + V_2[(C_2 - C_1)A]} \quad \textbf{(27)}$$

$\mathbf{C_1}$ is the matrix phase stiffness tensor, $\mathbf{C_2}$ is the inclusion stiffness tensor, $\mathbf{V_2}$ is the inclusion volume ratio and **A** is the strain concentration tensor.

For a composite system consisting of a single arbitrarily shaped inclusion perfectly bonded to the matrix, the dilute strain concentration tensor of the effective particle is given by [15]:

$$\mathbf{A^{(dil)} = \left[I + SC^{-1}(C_2 - C_1)\right]^{-1}} \quad \textbf{(28)}$$

where **I** is the fourth order unit tensor and **S** the fourth order Eshelby tensor.

Stress and strain concentration tensors relate the stress fields in the inhomogeneity and the matrix to the remote stress. As the inclusion volume fraction decreases, interaction between the inclusions reduces the accuracy of the dilute approximation (i.e. average strain fields in the matrix and the reinforcement are influenced by interactions of the strain fields between inclusions).

The Mori-Tanaka approach accounts for particle interactions where the strain concentration tensor **A** is given by [15]:

$$\mathbf{A = A^{(dil)}\left[V_1 I + V_2\left(A^{(dil)}\right)\right]^{-1}} \quad \textbf{(29)}$$

where $\mathbf{V_1}$ is the matrix volume ratio.

Wang and Pyrz [92] applied the Mori-Tanaka approach to predict the elastic properties of a composite material reinforced with randomly oriented transversely isotropic spheroids (montmorillonite silicate) with an arbitrary aspect ratio. It was observed that the aspect ratio has a considerable influence on the overall moduli, especially at small aspect ratio values. The overall moduli of the composite materials reinforced with transversely isotropic spheroids are primarily determined by the stiffness of the spheroids in the direction of the major axis, especially for the cases of small and large aspect ratios.

Brune and Bicerano [85] used the Halpin-Tsai equation to predict the modulus of a nanocomposite containing incompletely exfoliated stacks of clay platelets. In this case, pseudo-particles were used to represent the incompletely exfoliated stacks and included the inter-platelet spacing. The model was used to demonstrate the reduction of reinforcement efficiency of clay platelets of high aspect ratio in a polymer matrix as a result of incomplete exfoliation.

The modified Halpin-Tsai equation for tensile modulus of intercalated (or incompletely exfoliated) nanocomposites is given below [15, 85]:

$$\mathbf{E_c = E_m\left(\frac{1+\xi'\chi'\phi'}{1-\chi'\phi'}\right)} \tag{30}$$

where:

$$\chi' = \frac{\mathbf{E'_r - 1}}{\mathbf{E'_r + \xi'}} \tag{31}$$

where $\mathbf{E'_r}$ is the ratio of the modulus of the platelet stack to that of the matrix, $\xi'$ the aspect ratio of the platelet stack and $\phi'$ is the volume fraction of the platelet stacks in the matrix.

In each platelet stack, there are **N** platelet layers and various distances can separate the platelets within the stack from each other. The authors derived the following relationships between the aspect ratio $\xi$, $\mathbf{E_f}$ and $\phi_f$ for exfoliated and intercalated systems [85]:

$$\xi' = \frac{\xi}{\hat{N}}\left[\frac{1}{1+\left(1-1/\hat{N}\right)(s/t)}\right] \tag{32}$$

$$\phi' = \phi\left[1+\left(1-\frac{1}{\hat{N}}\right)\right]\frac{s}{t} \tag{33}$$

$$\mathbf{E'_r = E_r}\left[\frac{1}{1+\left(1-1/\hat{N}\right)(s/t)}\right] + \frac{\left(1-1/\hat{N}\right)(s/t)}{1+\left(1-1/\hat{N}\right)(s/t)} \tag{34}$$

$$\hat{N} = N + (1-N)\left(\frac{s}{t}\right)\left(\frac{\phi}{1-\phi}\right) \tag{35}$$

where $\mathbf{E_r}$ is the ratio of the platelet to the matrix modulus. In the case of either a single platelet (**N = 0**) or no inter-platelet layer (**s/t = 0**), the above relationships revert to the Halpin-Tsai equation. Brune and Bicerano [85] have suggested further refinements to the above analysis in order to correctly define the effects of the aspect ratio.

Li et al [93] used the Halpin-Tsai method to model the distribution of clay platelets. The average dimensions of platelet stacks required for the model were determined from TEM observations. A two-step approach was used – first the platelet stack was treated as a localised composite. Solutions from this analysis were then used with the Halpin-Tsai equation to obtain the elastic modulus of the overall composite. There was good correlation between predictions and experimental data from tensile and bend tests, although the model was only suitable for clay concentrations up to 30 wt.%, which is considerably greater than concentrations usually used in nanocoposites.

Thostenson and Chou [94] used an approach based on Halpin-Tsai to determine the effective elastic modulus of a nanocomposite consisting of aligned multi-walled carbon nanotubes embedded in a polystyrene matrix. The elastic modulus of the multi-walled nanotube was modelled by assuming that the outer wall acts as an effective solid fibre with the same diameter and length. An applied external force on the nanotube and fibre results in an iso-strain condition, which can be used to relate the elastic properties of the nanotube to the effective fibre. The Halpin-Tsai equation can then be used to predict the overall elastic properties of the polymer matrix with nanotube reinforcement. For multi-walled nanotubes there is typically a distribution of nanotube diameters in a sample. The authors also considered double Lorentz and Gauss distributions as probability density functions for the nanotube diameter distribution. This model has been used to show that the properties of nanotube composites are strongly influenced by the nanotube diameter. Experimental elastic modulus data were obtained for model composite systems, aligned nanocomposite films with 5 and 10wt% nanotubes. These data were compared with elastic modulus predictions using the micromechanics model. Predictions using the Lorentz distribution compares well while the Gauss distribution overestimates the composite modulus especially at higher loading fractions.

Multiple concentric cylinder assemblies have been used extensively in the literature [95-96] as the basis for modelling elastic properties of continuous unidirectional laminates, and for predicting the stress transfer that occurs following fibre fracture and transverse matrix cracking. In the concentric cylinder model, the fibre is represented by a cylinder, which is either singly embedded in a matrix cylinder or doubly embedded in concentric cylinders of increasing diameter representing the interphase and bulk matrix (Figure 21). The volume fractions of the composite in each cylinder remain constant.

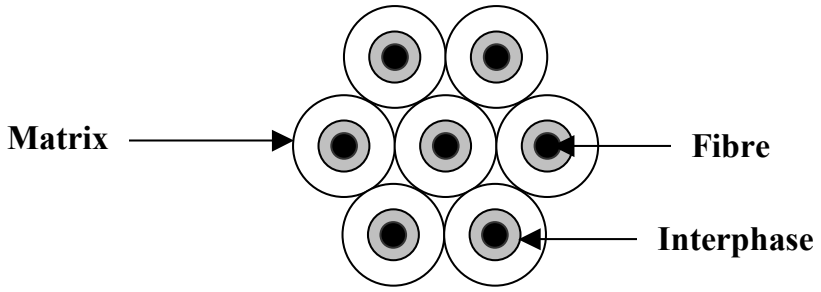


**Figure 21: Hexagonal fibre array depicting fibres with interphase and matrix**

In earlier approaches, the representative volume element (RVE) for a unidirectional laminate was considered to be a set of perfectly bonded coaxial cylinders. Hashin and Rosen [95-96] modelled a composite as an assembly of concentric cylinders, deriving lower and upper bounds for the elastic properties of unidirectional composites using extremum principles of minimum potential and minimum complementary energy, respectively. It was assumed that all constituents were linearly elastic, isotropic and homogeneous. Two fibre cases were considered. In the first case, the fibres were assumed to have identical cross-sectional area and form a hexagonal array in the transverse plane (Figure 21) and in the second, fibres were allowed to have different diameters and were randomly located in the transverse plane. In both cases, the ratio of inner to outer diameter was identical, and the composite was considered to be macroscopically homogeneous and transversely isotropic.

It was not obvious from the numerical study conducted by Hashin and Rosen [95], which of the two fibre arrays best represents a real composite. The random array is more representative of real composites, but insufficiently rigorous because of the geometric approximation of irregular fibre and interphase shapes by circles. However, good agreement between predicted and measured elastic properties has been achieved using the random fibre array [97-98].

Guzmán and Miravete [89] considered the fibre phase as a series of long circular concentric cylinders randomly distributed throughout the composite. The composite model consisted of three phases, a fibre surrounded by an annulus of matrix embedded in an equivalent homogeneous medium (i.e. surrounding composite). The authors derived equations for predicting Young's modulus and Poisson's ratio of a cluster. The model assumes that each cluster behaves like a homogeneous particle, and that the interactions between particles are negligible. An attempt was made to model the effective bulk modulus and effective shear modulus of a dilute suspension of elastic spherical particles in a continuous phase. The correlation between predictive analysis and experimental results was reasonable.

Micromechanics methods such as Halpin-Tsai do not include interface properties. In nanocomposites there are nanoscale interactions between the embedded nanotube and adjacent polymer chain leading to the formation of an interphase region. Experimentally it is very difficult to measure the mechanical properties of this interphase region due to the small length scale. Fisher et al [99] used a three-phase (fibre/nanotube – annular interphase – matrix) Mori-Tanaka micromechanics model to predict the properties of the interphase region from macroscale viscoelastic data. The Eshelby tensor was used as the dilute strain concentration tensor for ellipsoidal inclusions, the limiting case of which is an infinitely long cylindrical inclusion. If the Eshelby tensor were calculated for each of the three phases, this would represent a system where the interphase is separate to the fibre. Therefore the analytical solution was reformulated to produce a tensor for the case of an annular interphase surrounding the nanotube. An elastic analysis was used to predict the effective composite modulus for two cases - aligned fibres and randomly oriented fibres. The authors suggest this model could be extended to predict viscoelastic properties. This method could then be used with experimental data to infer the viscoelastic properties of the interphase.

A new multiphase concentric cylinder model (Figure 22) has been developed at NPL by L N McCartney [100] in which the concentric cylinders consist of different transverse isotropic materials having the same axis of symmetry that coincides with the axis of the cylinders. The model enables the stress and displacement distributions to be calculated for a set of perfectly bonded concentric cylinders subject to biaxial, axial shear and transverse shear loading. The cylinders are assumed to form a hexagonal array. The stress and displacement solutions can be used to calculate the effective thermoelastic properties for a unidirectional fibre-reinforced laminate given the thermoelastic properties for each cylinder of the assembly. The model accounts for thermally induced residual stresses and provides exact elasticity solutions. Predictions for a carbon fibre-reinforced epoxy composite were in good agreement with corresponding FEA calculations.

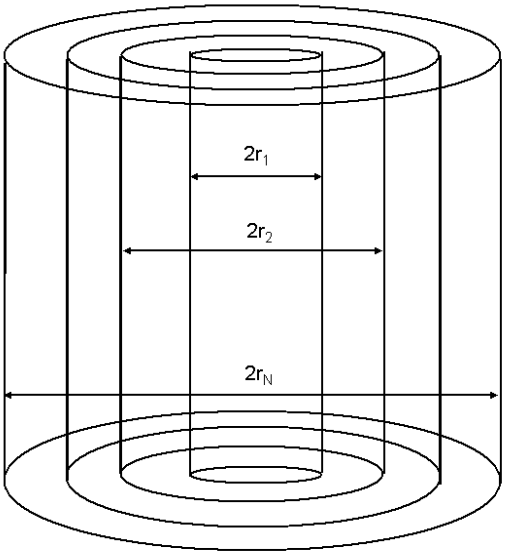


**Figure 22: Diagram showing concentric cylinder model**

An alternative approach, which takes account of the interface, is to use equivalent-continuum method (ECM) to model the nanotube, local polymer adjacent to the nanotube and the nanotube/polymer interface as an equivalent-continuum fibre. The mechanical properties of this RVE can be calculated through molecular modelling. This RVE can then be used as an effective fibre in a micromechanics analysis.

Odegard et al [101] used ECM to obtain a RVE for a polyimide/single-walled nanotube composite. The authors then used the Mori-Tanaka approach to predict the elastic properties of the composite at various lengths, orientations and volume fractions of nanotubes. The predicted values were larger than measured vales. The difference between experimental data and the model was thought to be due to the fact that the model assumes fibres are perfectly dispersed in the polymer matrix, while in reality a significant proportion of nanotubes remain in bundles in the composite material.

Buryachenko and Roy [102] used the ECM approach in conjunction with a one-particle approximation of the multiple-particle effective field method (MEFM) to predict elastic properties. This method allows for the interaction of particles within a nanocomposite and is based on homogeneous ellipsoidal inclusions. The method models the inclusion shape and the ellipsoidal spatial correlation of inclusion location (known as correlation holes). The authors used an orientation distribution function to represent the distribution of fibres. The model allowed consideration of both isotropic and transversely anisotropic fibres and was used to predict the effective longitudinal and transverse modulus of the composite as a function of volume concentration of fibres for 1-D, 2-D and 3-D random cases. Predictions were compared to those obtained using the Mori-Tanaka method. The MEFM estimations were found to agree well with the Mori-Tanaka predictions for the 1-D and 3-D cases.

Luo and Daniel [103] developed a three-phase model, which included polymer matrix, exfoliated nanolayers and nanolayer clusters. The region consisting of matrix with exfoliated nanolayers or platelets was analysed by assuming near uniform dispersion and random orientation. The properties of intercalated clusters of platelets were calculated by a rule of mixtures based on a parallel platelet system.

Mori-Tanaka method was used to calculate the modulus of the nanocomposite as a function of filler content for various material and geometric properties and microstructure/nanostructure morphology. The predictive analysis was in reasonable agreement with experimental results obtained for a nanoclay/epoxy system. Parametric studies were conducted to ascertain the effects of exfoliation ratio, clay layer and cluster aspect ratios, d-spacing, interlayer (intragallery) modulus, and the elastic modulus and Poisson's ratio of the matrix on the Young's modulus of the nanocomposite.

Chabert at al [104] used a four-phase spherical RVE for modelling the elastic response of rigid polystyrene particles randomly dispersed in a soft polybutylacrylate polymer matrix. It was assumed that nanocomposite materials consisted of submicron sized rigid particles randomly dispersed in the soft polymeric matrix. The RVE includes a shell representing the interphase between the filler particle and the surrounding polymer matrix. Two micromechanical models were proposed to account for short-range interactions between filler particles (self consistent scheme) and local filler/filler and filler/matrix contact (discrete assembly of sphere assembly). Numerical simulations carried out on a compact assembly of ~10000 mono disperse rigid spheres showed the model was in good agreement with experimental results and highlighted the importance of filler-filler interactions on the reinforcement above the percolation threshold.

McCartney and Kelly [105] have adapted the far-field methodology developed by Maxwell, when estimating the effective electrical conductivity of isotropic particulate composites, to estimate effective thermoelastic properties of multi-phase isotropic composites. Maxwell's methodology applied to the analogous thermal conduction problem is extended to multi-phase spherical particles having different sizes and properties. The methodology was used to estimate the effective bulk and shear moduli, and the coefficients of thermal expansion of multi-phase isotropic particulate composites. The results correspond with expressions derived in the literature, and coincide with, or lie between, variational bounds for all volume fractions. It was concluded that Maxwell's methodology is a unifying optimum technique to estimate the properties of multi-phase isotropic particulate composites, because it provides closed form estimates that are fully consistent with other methods, without imposing restrictions, except that the particles must be spherical (but can have a range of size and properties) and the resultant effective properties must be isotropic.

In a well-mixed cluster of **N** types of particulate reinforcement embedded in and perfectly bonded to an infinite matrix (see Figure 23), there are $\mathbf{n_i}$ spherical particles of radius $\mathbf{a_i}$, $\mathbf{i = 1 \ldots N}$ [105]. Particle properties of type **i**, which may differ from those of other types, are denoted by the superscript **i**. The cluster of all particle types may be just enclosed by a sphere of radius **b** and the particle distribution is homogeneous leading to isotropic effective properties of the composite formed by the cluster and matrix lying within this sphere. The packing density of the particles must not be so densely packed that the effective properties are anisotropic.

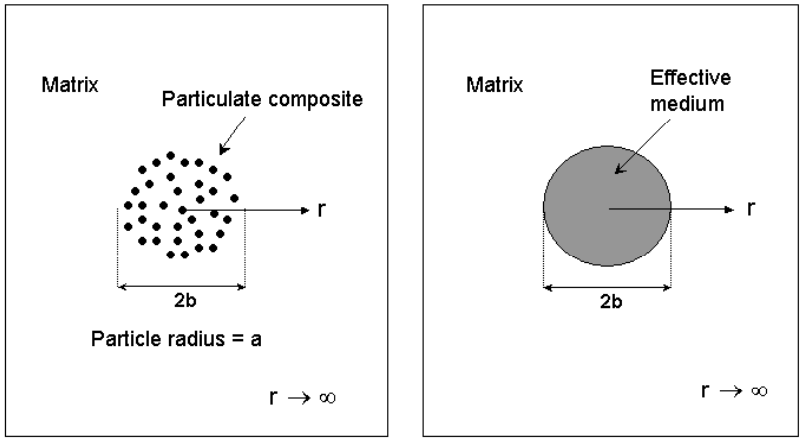


**(a) Discrete Model** **(b) Effective Medium Model**

**Figure 23: Particulate composite - spherical particles embedded in infinite matrix**

The volume fractions of particles of type **i** within the enclosing sphere of radius **b** are given by [105]:

$$V_p^i = n_i\left(\frac{a_i}{b}\right)^3, i = 1,...,N, \quad \text{such that } V_m + \sum_{i=1}^{N} V_p^i = 1 \tag{36}$$

where $V_m$ is the volume fraction of matrix. For one type of particle, with **n** particles of radius **a** within the enclosing sphere of radius **b**, the particulate volume fraction $V_p$ is such that [105]:

$$V_p = n_i\left(\frac{a}{b}\right)^3 = 1 - V_m \tag{37}$$

Whatever the nature and arrangement of spherical particles in the cluster, Maxwell's methodology considers the far-field when replacing the isotropic discrete particulate composite shown in Figure 23(a), that can be enclosed by a sphere of radius **b**, by an homogeneous effective composite sphere of the same radius **b** embedded in the matrix as shown in Figure 23(b). There is no restriction on sizes, properties and locations of particles provided that the equivalent effective medium is homogeneous and isotropic.

## 5.2 MOLECULAR MODELLING

Molecular modelling techniques are important in the prediction of physical material properties, such as elastic response, binding energies and atomic structure. As the technique models the discrete molecular structure, it is ideal for studying the atomic interactions at the nanoscale. However, these techniques can be computationally expensive, and therefore limited to small length and timescales. The three main molecular modelling techniques for the prediction of nanocomposites properties are molecular dynamics (MD) [106], Monte Carlo and ab initio simulation. Of these, molecular dynamics is the most widely used technique.

A combination of modelling techniques is usually required to simulate the bulk behaviour of nanocomposites. To scale up predictions from a molecular dynamic simulation ECM can be used [102]. An equivalent continuum, identical to the molecular dynamic model geometry, is developed and a constitutive law is used to describe the mechanical behaviour of the continuum. The energies of deformation of the MD and equivalent-continuum models are derived for identical loading conditions. The unknown mechanical properties of the equivalent-continuum are determined by equating the energies of deformation. The properties of a larger-scale material are then determined using the ECM element properties.

## 5.3 COMPUTATIONAL METHODS

Computational methods available to model nanocomposites are FEA and BEM. These methods provide numerical computation of bulk properties based on geometry, properties and volume fraction of constituent phases. The material RVE is discretized into elements for which the elastic solution leads to the determination of stress and strain fields. In FE analyses, the whole RVE is meshed with elements and the level of mesh refinement determines the predictive accuracy - ideally a fine mesh should be used to be able to capture the stress fields accurately. Where as in the boundary element method, elements are only used along the boundaries. The boundary integral equations (BIE's) are solved to evaluate the stress and strain fields. Hence, this method is less computationally expensive than FE methods.

Liu and Chen [107] have used both methods to model a carbon nanotube composite, although the BE method was the main focus of the work. For this BE method, the equation used was a weakly singular form of the conventional boundary integration equation and so did not involve computation of any singular integrals. This BIE can be applied to thin shell-like materials or structures, as long as the nearly singular integrals can be computed accurately and efficiently. The BIE is applied to the carbon nanotube and matrix separately and the resulting two equations are coupled at the interface. Perfect bonding is assumed between the nanotube and matrix. A square RVE with a single fibre was modelled as a BEM mesh and also an FE mesh. Two load cases were considered: bending loading to study deformation and axial loading to study the load transfer mechanisms. Good correlation was obtained between methods for both cases, although the BEM proved more efficient.

When modelling a large number of nanotubes the size of the FE and BEM models becomes more of an issue. A recent development in this area is the fast multipole boundary element method, which further improves the efficiency of the BEM. This method has been used by Liu et al [108] to obtain the effective modulus of a carbon nanotube composite. In this analysis, the nanotube was treated as a rigid fibre in an elastic matrix, with the assumption of perfect interfacial bonding. The fast-multipole BEM elements of integration are grouped together according to distance between the element and the source point. The integrations on elements in one cluster are computed together using multipole expansion therefore reducing computing time. Triangular elements were used to discretize the interface between the fibre and matrix. Two fibre orientations were studied; uniformly aligned and randomly aligned (fibres still aligned in x-direction but with no regular pattern). True random orientation could not be considered due to problems generating RVE models without causing contact of the fibres.

The authors used BEM to calculate the effective longitudinal modulus and compared results to those from the Halpin-Tsai method. The two methods compared well at low volume fractions. The effect of volume fraction of larger aspect ratio fibres on the effective modulus was studied using a refined mesh. The authors compared results with predictions obtained in earlier work using molecular dynamics combined with an equivalent continuum model, and to results from the Halpin-Tsai method. There was good correlation with the molecular dynamics method while the Halpin-Tsai method underestimates the effective modulus (probably due to the large aspect ration of the fibres). The authors suggest more realistic interface conditions based on molecular dynamics simulations could be incorporated into fast-multipole BEM.

Computational methods can also be utilised for studying different aspects of a nanocomposite, such as nanotube properties and interphase regions. Meo and Rossi [109] used an FE model based on molecular mechanics to obtain the Young's modulus of the nanotube itself. The authors used a combination of non-linear springs and torsional elastic springs to create a mesh of the nanotube based on the carbon-carbon model. Predicted nanotube modulus values were in good agreement with numerical and experimental data presented by other researchers.

Bogetti et al [110] used AFM to demonstrate that there is a property gradient throughout the interphase region between the nanofiller and the bulk matrix. Interphase properties of both an unsized and a sized carbon fibre were investigated. AFM measurements found that the interphase region for the unsized fibre was too small (relative to the size of the indentation probe) to characterise accurately. A 3-D FE model of the sized fibre composite was constructed. This incorporated the property gradient across the interphase through the use of a user-defined UMAT subroutine within the ABAQUS FE software package. The analysis was used to predict the indentation response along a radial line from the centre of a fibre. Good agreement was found between the FE predictions and the AFM measured values of stiffness at an ambient temperature.

## 6 DISCUSSION AND CONCLUSIONS

It was clearly evident from the review that only a few non-invasive techniques, such as XRD and TEM were potentially suitable for measuring the size (and distribution), shape (and distribution) and degree of dispersion of nanosized filler particles in polymeric systems and that these techniques were unsuitable for production and service inspection purposes. It is worth noting that progress has been made in developing portable XRD systems. In contrast, there were a large number of techniques that could indirectly provide information on particle shape, size and distribution, which relied on the material properties (e.g. flow, permittivity, electrical conductivity and ultrasonic transmission) being measured being sensitive to the dispersed phase size, shape and distribution. These measurements require independent confirmation using XRD and TEM and are limited by material type and scale. The equipment costs associated with many of the techniques was generally high, especially those techniques requiring UHV conditions. There were one or more techniques that with further development could prove invaluable to current and future research work.

**Optical Methods**: The number of optical microscopy techniques available is considerable. These techniques are generally used for imaging purposes providing information on surface topography (e.g. roughness), although techniques such as near field microscopy can be used to provide quantitative information on the size, shape, distribution and location of grains, particulates and defects, and phase changes. The spatial resolution (~10 μm) of these techniques, however, is inadequate for the purpose of measuring the dispersion of fillers with nanoscale dimensions. Light scattering techniques (e.g. DLS) have proved effective tools for measuring particle size and shape distributions, and degree of dispersion in liquid melts and have been adopted for quality assurance purposes in the manufacture of PNCs. These techniques have spatial resolutions of the order of 1-2 nm more than adequate for studying PNCs. Light absorbance and transmission spectra potentially could be used as a direct method of ascertaining the degree of exfoliation in transparent or semi-transparent nanocomposite products. The spatial resolution would be an issue, although use for production and in-service conditions would be possible as there are portable systems commercially available.

**Ultrasonic and Acoustic Methods:** A versatile group of techniques capable of providing information on microstructural features within the bulk of the material and elastic property data. Ultrasonic parameters, such as velocity, attenuation, scattering amplitude, scattering spectrum and frequency dependence are being used to provide information on a wide range of material properties. For example, ultrasonic velocities provide information relating to material composition and can be used to determine elastic properties. Scattering amplitude can be used to determine microstructure. It may be possible to differentiate between different degrees of crystallization, and hence degree of dispersion based on frequency or time dependence measurements. Laser ultrasonics has potential for real-time, in-situ microstructural measurements for monitoring/controlling processing. Although a number of proto-type systems have been developed there are no commercial systems available. In order to develop a working system, considerable capital outlay would be required. Data analysis and interpretation is also considerably complex.

A number of ultrasonic techniques could be investigated including scanning acoustic microscopy (SAM). The SAM system at NPL currently operates from 0 to 75 MHz. A frequency range of 200 MHz to 600 MHz would enable information to be obtained on micro-scale features down to approximately 2 microns suitable for use in studying material microstructures, although limited applicability to nanocomposites. The layer thickness and mechanical properties of layered solids could be studied by examining the dispersion properties of surface acoustic waves. The development of a high frequency bandwidth (GHz) ultrasonic system capable of measuring 3-D elastic properties and investigating internal structures (including damage) warrants further consideration. It would require capital investment in equipment in order to produce a system with a suitable bandwidth to enable determination of elastic properties and nanostructural differences.

**Electrical and Electromagnetic Techniques:** Although this group of techniques are used for NDE purposes, particularly for production, maintenance and service inspection there is potential for using one or more of these methods for determining the size (and distribution), shape (and distribution) and degree of dispersion of nanosized filler particles in polymeric systems.

The degree of dispersion of the nanoparticles is fundamental in determining the dielectric behaviour. Clustering (particle agglomeration) can be expected to result in local modifications of the electrical conductivity and admittance. It is possible to differentiate between the nanocomposite and base resin from the plots of loss tangent and real part of the relative permittivity. Tapered dielectric waveguide probes are capable of mapping the spatially varying dielectric properties of materials with a spatial resolution of better than 500 μm. EID is is able to provide images of the conductivity or permittivity of a component inferred from surface electrical measurements. As previously mentioned, eddy current increases with increasing conductivity, and therefore these techniques are not particularly suited to non-metallic substrates, thus limiting their applications.

**X-Ray Techniques**: A powerful collection of techniques capable of providing detailed information relating to microstructure, composition and residual stress state. As shown in Sections 4.1 and 4.2, the potential for these techniques is immense. The two techniques that stand out are XRD and X-ray tomography. XRD systems are now capable of providing key information regarding the microstructure, size and distribution of nanoparticles and micro-chemical composition analysis (20 μm square inspection area). Interpretation of XRD data is difficult and susceptible to error. Further work is required to establish a relationship between the XRD measurements and dimensions of nanoscale features, such as interlayer spacing and platelet thickness of intercalated clay-based PNCs. This would require accurate calibration specimens. X-ray tomography can provide 3-D microstructural information. Although the technique is a powerful and versatile inspection tool, its main drawback at present is its high investment cost and limited resolution (10 μm) with respect to length-scale associated with nanocomposites.

**Scanning Probe Microscopy (SPM):** SPM consists of a powerful set of techniques, such as AFM and nanoindentation, which could potentially provide quantitative data on the size (and distribution), shape (and distribution) and degree of dispersion of nanosized filler particles in polymeric systems. SPM techniques are not restricted by material type or format, or limited to ambient conditions, and thus could be used for sub-zero and elevated temperature studies. The review identified a number of issues still to be resolved with both AFM and nanoindentation in order to provide the necessary confidence in the use of these techniques in providing accurate and reliable engineering data. There is a high degree of uncertainty in the measured data, which can be attributed to a number of factors, such as load frame compliance correction, calibration errors, difficulty in establishing true zero for load and displacement, variability in probe tip geometry, wear and deformation of indenter tip, surface roughness effects, thermal drift and vibration effects. All these issues need to be addressed in a rigorous and controlled manner in order to formalise methods based on these surface techniques for nanoscale measurements.

**Spectroscopy and Chromatography Techniques**: These techniques can provide important information on surface and bulk physical-chemical characteristics of materials both at the surface and within the bulk. Major concerns with most of these techniques relate to the need for UHV conditions and the high capital equipment outlay required and high maintenance costs. IRS and Raman Spectroscopy (see optical techniques) are two techniques that are not restricted by the need for UHV conditions.

Raman spectroscopy is sensitive to a material's composition and structure and can distinguish between different structural arrangements of similar atoms. The spatial resolution is limited to a few microns. IRS can provide chemical composition information on PNCs and constituents. It is possible to determine the formation/transformation of chemical species in polymeric materials during cure, providing direct information about the timescale within which the chemicals involved in the cure reaction have been used and the reaction is complete. The technique can be used to analyse gases, liquids and solids. Combined with dielectrics and other techniques it could be used to assess the effect of dispersion on the rheological behaviour of polymer melts.

**Rheometry:** The flow of multi-phase polymeric systems is sensitive to the dispersed phase size, shape and surface characteristics, as well as degree of dispersion and particle/particle and particle/matrix interactions. Rheological measurements can provide correlations between molecular structure and material properties, and between material properties and behaviour in practical situations, such as on-line quality inspection of production. Measurement of the key rheological characteristics can provide valuable information on global exfoliation and the percolation threshold.

**It is recommended that dielectric and ultrasonic techniques be pursued further in-depth**. These techniques are potentially capable of being used in the field for production and service inspection. Exploratory work should also be carried out to assess the suitability of light transmission and absorption measurements as an indirect approach for determining degree of dispersion (exfoliation). In order to facilitate this exercise, it is recommended that XRD, TEM, DLS and rheometric measurements be performed in order to verify measurements obtained by the above-mentioned techniques. DLS and rheometry being techniques best suited to measure dispersion in polymer melts.

Although ultrasonic techniques (e.g. laser-ultrasound) are potentially suitable for in-situ microstructure measurements, it would require a significant capital outlay in addition to considerable time and effort to design and assemble an ultrasonic system, and produce reliable data. Data interpretation is difficult requiring an expert knowledge of both ultrasonics and materials. Case studies would need to be defined and tests conducted on materials with known microstructure to assess the sensitivity and resolution of the techniques to be followed by further assessment on materials whose detailed microstructure is unknown. The actual microstructure of the material would be determined subsequently using conventional techniques, such as XRD and TEM.

**A common issue with most of these techniques is that there is a need for further work in establishing procedures for ensuring accurate and repeatable measurements that represent actual material properties.**

**Modelling:** Molecular dynamics simulations [106] have provided a critical insight into the complex dynamic behaviour of nanocomposites, such as nanoclays. The molecular dynamic approach is a well-known method used to simulate chemical and physical properties of structures at the atomic-scale level. A simpler approach is to simulate the overall mechanical deformation of nanofillers (i.e. nanotubes) using elastic rods and beams (i.e. continuum mechanics and shell theory), provided the aspect ratio of the nanoparticles is greater than $10^3$.

Micromechanical models, such as Halpin-Tsai and Mori-Tanaka models developed for conventional composites are commonly used for modelling the elastic properties of PNCs. The Halpin-Tsai method is a semi-empirical approach relying on experimental data in order to generate reinforcing (or scaling) factors, which could be modified to allow for different degrees of dispersion and interfacial strength. Mori-Tanaka mean field theory is a further refinement of micromechanical modelling, which has been used with some success in predicting the elastic properties of a composite material reinforced with randomly oriented transversely isotropic spheroids (montmorillonite silicate) with an arbitrary aspect ratio. It has been incorporated into numerical simulations of multi-particle systems (ca. 10000 particles) to model the effects of clustering and component interactions.

Maxwell's far-field methodology for estimating the effective electrical conductivity of isotropic particulate composites may also be used to estimate the effective bulk and shear moduli, and the coefficient of thermal expansion. The approach enables the consideration of multi-phase composites having distributions of both particle sizes and properties, and has been shown to be valid for a wide range of volume fractions. It does not impose restrictions, except that the particles must be spherical (but can have a range of sizes and properties), and the resultant effective properties must be isotropic. Recent developments are underway to extend the model to include cylindrical and spheroidal particle geometries. The issue arises as to validation of the model for partially or poorly bonded systems and the ability of the model to accommodate non-uniform dispersion observed in actual composites. It may be possible to modify the model to include an interphase region and to provide the necessary input data using AFM and nanoindentation techniques discussed previously in order to verify the applicability of the model for these systems.

If the behaviour of this interphase region in nanocomposites is to be considered then the molecular modelling approach is the most accurate. But this approach is complex, computationally very expensive and is hence limited to small length scales. Another approach is to use an equivalent-continuum model based on molecular modelling predictions to obtain a representative volume element, which can be used in a micromechanics analysis. Alternatively, micromechanics models such as Mori-Tanaka can be reformulated to include an interphase region, which removes the molecular modelling requirement. As computing power becomes cheaper, computational methods are becoming more attractive. If the interphase region can be characterised a FE mesh can be created with a defined interphase region, and appropriate material properties. The use of a user subroutine even allows for the variation of properties across an interphase.

**Modelling deformation and failure of nanocomposites is still in its infancy. Future developments will need to account for a number of factors, including translational and rotational deformation of the nanoparticles, effects of clustering and interfacial properties (i.e. stress transfer, adhesion, and bond strength).**

**ACKOWLEDGEMENTS**

This work was funded by the United Kingdom Department for Innovation, University and Skills (National Measurement System Policy Unit) as part of the Thermal and Materials Metrology Programme (2007- 2010). The author would like thank colleagues at the National Physical Laboratory particularly Dr Louise Crocker, Dr Neil McCartney, Dr John Nunn and Dr Martin Rides.

**REFERENCES**

1. Vaia, R.A. and Wagner, D.H., "Framework for Nanocomposites", Materials Today, November 2004, pp 32-37.
2. Lau, K-T., Chipara, M., Ling, H-Y and Hui, D., "On the Effective Elastic Moduli of Carbon Nanotubes for Nanocomposite Structures", Composites Part B, Volume 35, Number 2, 2004, pp 95-101.
3. Wagner, D.H and Vaia, R.A., "Nanocomposites: Issues at the Interface", 2004, pp 38-42.
4. Beyert, G., "Nanocomposites: A New Class of Flame Retardants for Polymers", Plastics, Additives and Compounding Journal, Volume 4, Part 10, 2002, pp 22-28.
5. Hong, I.J., Schadler, L.S., and Siegel, R.W., Rescaled Electrical Properties of ZnO/Low Density Polyethylene, Applied Physics Letters, Volume 82, pp 1956-1958.
6. Nelson, J.K. and Hu, Y., "Nanocomposite Dielectrics – Properties and Implications", Journal of Physics D: Applied Physics, Volume 38, 2005, pp 213-222.
7. Trias, D., Garcia, R., Costa, J., Blanco, N. and Hurtado, J.E., "Quality Control of CFRP by Means of Digital Image Processing and Statistical Point Pattern Analysis", Composites Science and Technology, Volume 67, 2007, pp 2438-2446.
8. Chen, X-M., Woodward M.B. and Papathanasiou, T.D., "Fiber Clustering: Its Quantification and Influence on the Permeability of Unidirectional Fibrous Media", Paper 56, Proceedings of SAMPE '07 Conference: M&P – Coast to Coast and Around the World, Volume 52, Baltimore, Maryland, USA, 3-7 June, 2007.
9. Diggle, P.J., "Statistical Analysis of Spatial Point Patterns", Arnold, 2003.
10. Pyrz, R., "Quantitative Description of the Microstructure of Composites. Part 1: Morphology of Unidirectional Composite Systems", Composites Science and Technology, Volume 50, 1994, pp 197-208.
11. Eberhardt, C. and Clarke, A., "Fibre-Orientation Measurements in Short-Glass Fibre Composites. Part I: Automated, High-Angular-Resolution Measurement by Confocal Microscopy", Composites Science and Technology, Volume 61, 2001, pp 1389-1400.
12. Eberhardt, C., Clarke, A., Vincent, M., Giroud, T. and Flouret S., "Fibre-Orientation Measurements in Short-Glass Fibre Composites. II: A Quantitative Error Estimate of the 2D Image Analysis Technique", Composites Science and Technology, Volume 61, 2001, pp 1961-1974.
13. Wang, S., Liang, Z., Wang, B. and Zhang, C., "Statistical Characterization of Single-Wall Carbon Nanotube Length Distribution", Nanotechnology, Volume 17, 2006, pp 634-639.

14. Utracki, L.A., “Clay-Containing Polymeric Nanocomposites”, Volume 1, Rapra Technology Limited, 2004.
15. Tjong, S.C., “Structural and Mechanical Properties of Polymer Nanocomposites”, Materials Science and Engineering, R 53, 2006, pp 73-197.
16. “Polymer Nanocomposites”, Editor Mai, Y-W. and Yu, Z-Z., Chapter 7, “Clay-Acrylate Nanocomposite Photopolymers”, Woodhead Publishing Limited, 2006.
17. Decker, C., Keller, L., Zahouily, K. and Benfarhi, S., “Synthesis of Nanocomposite Polymers by UV-Radiation Curing”, Polymer, Volume 46, 2005, pp 6640-6648.
18. Friedbacher, G. and Fuchs, H., “Classification of Scanning Probe Microscopies”, Pure Applied Chemistry, Volume 71, Number 7, 1999, pp 1337-1357.
19. Rabe, U. and Arnold, W., “Acoustic Microscopy by Atomic Force Microscopy”, Applied Physics Letters, Volume 64, Number 12, 1994, pp 1493-1495.
20. Rabe, U., Scherer, V., Hirsekorn, S., and Arnold, W., “Nanomechanical Surface Characterization by Atomic Force Acoustic Microscopy”, Journal of Vacuum Science Technology, Volume 15, Number 4, 1997, pp 1506-1511.
21. VanLandingham, M.R., Villarrubia, J.S., Guthrie, W.F. and Meyers, G.F., “Nanoindentation of Polymers: An Overview”, Macromolecular Symposium, Number 167, 2001, pp 15-43.
22. Binning, G. and Quate, C.F., “Atomic Force Microscope”, Physical Review Letters, Volume 56, Number 9, 1986, pp 930-933.
23. Maudgal, S., Sims, G.D., Johnstone, J.E. Jennett, N.M., “Characterisation of Surface Roughness of Fibres by Atomic Force Microscopy”, NPL Measurement Note CMMT (MN) 024, 1998.
24. Munz, M., Sturm, H., Schulz, E. and Hinrichsen, G., “The Scanning Force Microscope as a Tool for the Defection of Local Mechanical Properties Within the Interphase of Fibre Reinforced Polymers”, Composites Part A, Volume 29A, 1998, pp 1251-1259.
25. Mai, K., Mader, E. and Muhle, M., “Interphase Characterization in Composites with New Non-Destructive Methods”, Composites Part A, Volume 29A, 1998, pp 1111-1119.
26. VanLandingham, M.R., Dagastine, R.R., Eduljee, R.F., McCullough, R.L. and Gillespie Jr, J.W., “Characterization of Nanoscale Property Variations in Polymer Composite Systems: 1. Experimental Results”, Composites Part A, Volume 30, 1999, pp 75-83.
27. Syed Asif, S.A., Colton, R.J. and Wahl, K.J., “Nanoscale Surface Mechanical Property Measurements: Force Modulation Techniques Applied to Nanoindentation”, Interfacial Properties on the Submicron Scale”, Editors J Frommer and R Overney, ACS Books, 2000.
28. Higgins, M.J., Riener, R.K., Uchihashi, T., Sader, J.E., McKendry, R. and Jarvis, S.P., “Frequency Modulation Atomic Force Microscopy: A Dynamic Measurement Technique for Biological Systems”, Nanotechnology, Volume 16, 2005, pp S85-S89.
29. Hurley, D.C., Shen, K., Jennett, N.M. and Turner, J.A., “Atomic Force Acoustic Microscopy Methods to Determine Thin-Film Elastic Properties”, Journal of Applied Physics, Volume 94, Number 4, 2005, pp 2347-2354.
30. Hurley, D.C., Kopycinska-Muller, M., Kos, A.B. and Geiss, R.H., “Nanoscale Elastic-Property Measurements and Mapping Using Atomic Force Acoustic Microscopy Methods”, Measurement Science and Technology, Volume 16, 2005, pp 2167-2172.

31. Kopycinska-Muller, M., Geiss, R.H., Muller, J. and Hurley, D.C., "Elastic-Property Measurements of Ultrathin Films Using Atomic Force Acoustic Microscopy", Nanotechnology, Volume 16, 2005, pp 703-709.
32. Muller, R.H. and Mehnert, W., "Particle and Surface Characterisation Methods", Medpharm Scientific Publishers, 1999.
33. Bubert, H. and Jenett, H., "Surface and Thin Film Analysis", Wiley-VCH, 2002.
34. Gee, M.G. and Jennett, N.M., "An Introduction to the Mechanical Testing of Coatings", NPL Measurement Good Practice Guide 83, 2005.
35. Jennett, N.M., "An Introduction to Instrumented Indentation Testing", NPL Measurement Good Practice Guide 92, 2006.
36. BS EN ISO 14577-2: 2002, "Metallic Materials. Instrumented Indentation Test for Hardness and Materials Parameters. Verification and Calibration of Testing Machines".
37. Oliver, W.C. and Pharr, G.M., "An Improved Technique for Determining Hardness and Elastic Modulus Using Load and Displacement Sensing Indentation Experiments", Journal of Materials Research, Volume 7, 1992, pp 1564-1583.
38. Sneddon, I.N., "Boussinesq's Problem for a Rigid Cone", Proceedings of Cambridge Philosophical Society, Volume 44, 1948, pp 492-507.
39. Sneddon, I.N., "The Relation Between Load and Penetration in the Axisymmetric Baussinesq Problem for a Punch of Arbitrary Profile", International Journal of Engineering Science, Volume 3, 1965, pp 47-57.
40. Bouzakis, K –D., Michailidis, N., Hadjiyiannis, S., Skordaris, G. and Erkens, G., "The Effect of Specimen Roughness and Indenter Tip Geometry on the Determination Accuracy of Thin Hard Coatings Stress-Strain Laws by Nanoindentation", Materials characterization, Volume 49, 2003, pp 149-156.
41. Lodeiro M.J. and Mulligan, D.R., "Cure Monitoring Techniques for Polymer Composites, Adhesives and Coatings", NPL Good Practice Guide No 75, 2005.
42. Gower, M.R.L., Shaw, R.M. and Sims, G.D., "Good Practice Guide for the Assessment of Damage Tolerance Under Long-Term Loading", NPL Measurement Good Practice Guide No 101, 2007.
43. Broughton, W.R. and Dean, G.D., "Fatigue and Creep Testing of Adhesives and Thermoplastic Joined Systems", NPL Measurement Good Practice Guide No 104, 2007.
44. Van Krevelen, D.W., "Properties of Polymers", Elsevier, 1997.
45. Konscher, A.K., "Dielectric Relaxation in Solids", Journal of Physics D: Applied Physics, 1999, pp R57-R70.
46. Bellucci, F., Valentino, M., Monetta, T., Nicodemo, L., Kenny, J., Nicolais, L. and Mijović, J., "Impedance Spectroscopy of Reactive Polymers-1", Journal of Polymer Science B: Polymer Physics Volume 32, Issue 15, 1994, pp 2519-2527.
47. Wu, J. and Kong, L., "High Microwave Permittivity of Multiwalled Carbon Nanotube Composites", Applied Physics letters, Volume 84, Number 24, 2004, pp4956-4958.
48. Tjong, S.C., Liang, G.D. and Bao, S.P., "Electrical Behavior of Polypropylene/Multiwalled Carbon Nanotube Nanocomposites with Low Percolation Threshold", Scripta Materialia, Volume 57, 2007, pp 461-464.
49. Dang, Z-M., Yao, S-H. and Xu, H-P., "Effect of Tensile Strain on Morphology and Dielectric Property in Nanotube/Polymer Nanocomposites", Applied Physics Letters, Volume 90, Issue 1, 012907, 2007.

50. Nelson, J.K. and Hu, Y., "Nanocomposite Dielectrics – Properties and Implications", Journal of Physics D: Applied Physics, Volume 38, 2005, pp 213-222.
51. Lodeiro, M.J. and Hobbs, C., "Ultrasonic Measurements for Cure Monitoring in Polymeric Material Systems", NPL Measurement Note MATC (MN) 47, 2003.
52. Read, B.E. and Dean, G.D., "The Ultrasonic Immersion Method. The Determination of Dynamic Properties of Polymers and Composites", Adam Hilger Ltd, 1978, pp 156-179.
53. Papadakis, E.P., Patton, T., Tsai, Y-M., Thompson, D.O and Thompson, R.B., "The Elastic Moduli of a Thick Composite as Measured by Ultrasonic Bulk Wave Pulse Velocity", Journal of Acoustic Society of America, Volume 89, Number 6, 1991, pp 2753-2757.
54. Stijnman, P.W.A., "Determination of the Elastic Constants of Some Composites by Using Ultrasonic Velocity Measurements", Composites, Volume 26, 1995, pp 597-604.
55. Lu, X., Kim, K.Y. and Sachse, W., "In Situ Determination of Elastic Stiffness Constants of Thick Composites", Composites Science and Technology, Volume 57, 1997, pp 753-762.
56. Scruby, C.B. and Drain, L.E., "Laser-Ultrasonic: Techniques and Applications", Adam Hilger, 1990.
57. Davies, S.J., Edwards, C., Taylor, G.S. Palmer, S.B., "Laser Generated Ultrasound: Its Properties, Mechanisms and Multifarious Applications", Journal of Physics D: Applied Physics, Volume 26, 1993, pp 329-348.
58. Müller, R.H. and Mehnert, W., "Particle and Surface Characterisation Methods", Medpharm Scientific Publications, 1999.
59. Du, F., Scogna, R.C., Zhou, W., Brand, S., Fischer, J.E., and Winey, K.I., "Nanotube Networks in Polymer Nanocomposites: Rheology and Electrical Conductivity", Macromoleccules, Volume 37, 2004, pp 9048-9055.
60. ISO 13468 Parts 1 and 2:1999, "Plastics - Determination of the Total Luminous Transmittance of Transparent Materials".
61. ISO 14782:1999, "Plastics - Determination of Haze for Transparent Materials".
62. Clarke, P.J., "Regular Transmittance Measurements", NPL Measurement Good Practice Guide No 97, 2006.
63. Chunnilall, C.J., Deadman, A.J., Crane, L. and Usadi, E., "NPL Scales For Radiance Factor and Total Diffuse Reflectance, Metrologia, Volume 40, 2003, pp S192-S195.
64. ISO 6721, "Plastics - Determination of Dynamic Mechanical Properties".
65. Mulligan, D., Gnaniah, S. and Sims, G.D., "Thermal Analysis Techniques for Composites and Adhesives (Second Edition)", NPL Measurement Good Practice Guide No 62, 2003.
66. Sims, G.D. and Gnaniah, S., "Polymer Composites - Rate Dependent Temperature Calibration of Dynamic Mechanical Analysers (DMA) for Tg Measurements", NPL Measurement Note DEPC (MN) 017, 2005.
67. Meneghetti, P. and Qutubuddin, S., "Synthesis, Thermal Properties and Applications of Polymer-Clay Nanocomposites", Thermochimica Acta, Volume 442, 2006, pp 74-77.
68. Manias, E., Touny, A., Wu, L., Strawhecker, K., Lu, B., and Chung, T.C., "Polypropylene/Montmorillonite Nanocomposites. Review of the Synthetic Routes and Materials Properties", Chemical Materials, Volume 13, 2001, pp 3516-3523.

69. Giannelis, E.P., Krishnamoorti, R. and Manias, E., "Polymer-Silicate Nanocomposites: Model Systems for Confined Polymers and Polymer Bushes", Advances in Polymer Sciences, Volume 138, 1999, pp 107-147.
70. ISO 11357:1997, "Plastics – Differential Scanning Calorimetry (DSC)".
71. Rides, M., Allen, C., Dawson, A. and Nottay, J., "Surface Tension and Extrusion-Based Rheological Characterisation of Hot Melt Adhesives", NPL Measurement Good Practice Guide No 81, 2005.
72. Rides, M., "Rheological Characterisation of Filled Materials: A Review", NPL Measurement Note DEPC MPR 013, 2005.
73. Lee, K.M. and Han, C.D., "Effect of Hydrogen Bonding on the Rheology of Polycarbonate/Organoclay Nanocomposites", Polymer, Volume 44, 2003, pp 4573-4588.
74. Wagener, R. and Reisinger, T.J.G., "A Rheological Method to Compare the Degree of Exfoliation of Nanocomposites", Polymer 44, 2003, pp 7513-7518.
75. Zhao, J., Morgan, A.B. and Harris, J.D., "Rheological Characterization of Polystyrene-Clay Nanocomposites to Compare the Degree of Exfoliation and Dispersion", Polymer, Volume 46, 2005, pp 8641-8660.
76. Durmus, A., Kasgoz, A., Macosko, C.W., "Linear Low Density Polyethylene (LLDPE)/Clay Nanocomposites. Part I: Structural characterisation and Quantifying Clay Dispersion by Melt Rheology", Polymer, Volume 48, 2007, pp 4492-4502.
77. ISO 11443, "Plastics – Determination of Fluidity of Plastics Using Capillary and Slit-Die Rheometers".
78. ISO 3219:1993, "Plastics - Polymers/Resins in the Liquid State or as Emulsions or Dispersions - Determination of Viscosity Using a Rotational Viscometer with Defined Shear Rate".
79. ISO 6721-10: "Plastics - Determination of Dynamic Mechanical Properties, Part 10: Dynamic Shear Viscosity Using a Parallel Plate Oscillatory Rheometer".
80. BS 5168:1975. "Glossary of Rheological Terms".
81. Summerscales, J. and Short, D., "Chemical Spectroscopy", Chapter 7, Non-Destructive Testing of Fibre-Reinforced Plastic Composites, Volume 1, Editor Summerscales, J., Elsevier Applied Science, 1987.
82. Halpin, J.C. and Tsai, S.W., "Effects of Environmental Factors on Composite Materials", Airforce Materials Laboratory Technical Report AFML-TR67-243, 1969.
83. Halpin, J.C., "Stiffness and Expansion Estimates for Oriented Short Fiber Composites", Journal of Composite Materials", Volume 3, 1969, pp 732-734.
84. Halpin, J.C. and Kardos, J.L., "Strength of Discontinuous Reinforced Composites: I. Fiber Reinforced Composites", Polymer Engineering and Science, Volume 18, Number 6, 1978, pp 496-504.
85. Brune, D.A. and Bicerano, J., "Micromechanics of Nanocomposites: Comparison of Tensile and Compressive Elastic Moduli, and Prediction of Effects of Incomplete Exfoliation and Imperfect Alignment on Modulus", Polymer, Volume 43, 2002, pp. 369-387.
86. Thostenson, E.T. and Chou, T-W., "On the Elastic Properties of Carbon Nanotube-Based Composites: Modelling and Characterisation", Journal of Physics D: Applied Physics, Volume 36, 2003, pp. 573-582.
87. Sheng, N., Boyce, M.C., Parks, D.M., Rutledge, G.C., Abes, J.I. and Cohen, R.E., "Multiscale Micromechanical Modeling of Polymer/Clay Nanocomposites and the Effective Clay Particle", Polymer, Volume 45, 2004, pp 487-506.

88. Vlasveld, D.P.N., Groenewold, J., Bersee, H.E.N., Mendes, E. and Picken, S.J., "Analysis of the Modulus of Polyamide-6 Silicate Nanocomposites Using Moisture Controlled Variation of the Matrix Properties", Polymer, Volume 46, 2005, pp 6102-6113.
89. Guzmán de Villoria, R. and Miravete, A., "Mechanical Model to Evaluate the Effect of the Dispersion in Nanocomposites", Acta Materialia, Volume 55, 2007, pp 3025-3031.
90. Eshelby, J.D. "The Determination of the Elastic Field of an Ellipsoidal Inclusion and Related Problems", Proceedings Royal Society A, Volume 241, 1957, pp 376–396.
91. Duan, H.L. Wang, J, Huang, Z.P. and Karihaloo, B.L., "Eshelby Formalism for Nano-Inhomogeneities", Proceedings Royal Society A Volume 461, 2005, pp 3335–3353.
92. Wang, J. and Pyrz, R., "Prediction of the Overall Moduli of Layered Silicate-Reinforced Nanocomposites – Part I: Basic Theory and Formulas", Composites Science and Technology, Volume 64, 2004, pp 925-934.
93. Li, X., Gao, H., Scrivens, W.A., Fei, D, Thakur, V., Sutton, M.A., Reynolds, A.P. and Myrick, M.L., "Structural and Mechanical Characterization of Nanoclay-Reinforced Agarose Nanocomposites", Nanotechnology, Volume 16, 2005, pp. 2020-2029.
94. Thostenson, E.T. and Chou, T-W., "On the Elastic Properties of Carbon Nanotube-Based Composites: Modelling and Characterisation", Journal of Physics D: Applied Physics, Volume 36, 2003, pp. 573-582.
95. Hashin, Z. and Rosen, B.W., "The Elastic Moduli of Fiber-Reinforced Materials", Journal of Applied Mechanics, Volume 31E(2), 1964, pp 223-232.
96. Hashin, z., "On Elastic Behaviour of Fibre Reinforced Materials of Arbitrary Transverse Phase Geometry", Journal of Mechanics and Physics of Solids", Volume 13, 1965, pp 119-134.
97. Hult, J. and Rammerstorfer, F.G., "Engineering Mechanics of Fibre Reinforced Polymers and Composite Structures", Springer Verlag, 1994.
98. Song, Y.S. and Youn, J.R., "Modeling of Effective Elastic Properties for Polymer Based Carbon Nanotube Composites", Polymer, Volume 47, 2006, pp 1741-1748.
99. Fisher, F.T., Lee, K-C and Brinson, L.C., "Elastic and Viscoelastic Properties of Non-Bulk Polymer Interphases in Nanotube-Reinforced Polymers", Proceedings of SEM 2005 Annual Conference on Experimental and Applied Mechanics, June 7-9, Portland, USA.
100. McCartney, L.N., "Recursive Method of Calculating the Effective Thermoelastic Constants for Systems of Axi-Symmetric Concentric Cylinders", to be published.
101. Odegard, G.M., Gates, T.S., Wise, K.E., Park, C. and Siochi, E.J., "Constitutive Modelling of Nanotube-Reinforced Polymer Composites", Composites Science and Technology, Volume 63, 2003, pp. 1671-1687.
102. Buryachenko, V.A. and Roy, A., "Effective Elastic Moduli of Nanocomposites with Prescribed Ransom Orientation of Nanofibres", Composites: Part B, Volume 36, 2005, pp. 405-416.
103. Luo, J-J. and Daniel, I.M., "Characterization and Modelling of Mechanical Behavior of Polymer/Clay Nanocomposites", Composites Science and Technology, Volume 63, 2003, pp 1607-1616.

104. Chabert, E., Dendievel, R., Gauthier, C. and Cavaillé, J.-Y., "Prediction of the Elastic Response of Polymer Based Nanocomposites: A Mean Field approach and a Discrete Simulation", Composites Science and Technology, Volume 64, 2004, pp 309-316.
105. McCartney, L.N. and Kelly, A., "Maxwell's Far-Field Methodology Applied to the Prediction of Properties of Multi-Phase Isotropic Particulate Composites", Proceedings of Royal Society. A, Volume 464, 2008, pp 423-446.
106. Cho, J., Luo, J.J. and Daniel, I.M., "Mechanical Characterization of Graphite/Epoxy Nanocomposites by Multi-Scale Analysis", Composites Science and Technology, Volume 67, 2007, pp 2399-2407.
107. Liu, X.Y. and Chen, X.L., "Continuum Models of Carbon Nanotube-Based Composites Using the Boundary Element Method", Electronic Journal of Boundary Elements, Volume 1, Number 2, 2003, pp. 316-335.
108. Liu, Y., Nishimura, N. and Otani, Y., "Large-Scale Modelling of Carbon-Nanotube Composites by a Fast Multipole Boundary Element Method", Computational Materials Science, Volume 34, 2005, pp. 173-187.
109. Meo, M. and Rossi, M., "Prediction of young's Modulus of Single Wall Carbon Nanotubes by Molecular-Mechanics Based Finite Element Modelling", Composites Science and Technology, Volume 66, 2006, pp. 1597-1605.
110. Bogetti, T.A., Wang, T., VanLandingham, M.R. and Gillespie Jr, J.W., "Characterization of Nanoscale Property Variations in Polymer Composite Systems: 2. Numerical Modelling", Composites: Part A, Volume 30, 1999, pp. 85-94.